Numerical modelling of large-scale finned tube latent thermal energy storage systems

J. Vogel[*], M. Keller, M. Johnson

German Aerospace Center (DLR), Pfaffenwaldring 38-40, 70569 Stuttgart, Germany

Abstract

In latent thermal energy storage, heat is transferred between a single- or two-phase heat transfer fluid and a solid/liquid phase change material. Due to the low thermal conductivity of most suitable storage materials, heat exchangers with highly thermally conductive fin structures are used to obtain feasible heat transfer rates. To study and optimize the performance of latent thermal energy storage systems, simulation models applicable on a large-scale level are required. However, the modeling of such a system in detail requires high computational effort. To overcome the current limitations of such models, a simplified and fast model for large-scale industrial storage systems is proposed in this work. The model was implemented with a self-tailored MATLAB code and consists of two coupled parts: the heat transfer fluid region and the storage region, which includes the phase change material and the heat exchanger. The heat transfer fluid region is modeled with quasi-stationary one-dimensional single- or two-phase flow models and constitutive equations for pressure drop and heat transfer. Material properties of liquid thermal oil and two-phase water/steam are used. The heat transfer fluid model was verified using simulation results obtained with the commercial software Apros. The storage region was modeled based on the transient energy equation and a phase change model on a structured cylindrical geometry. To efficiently include the effect of the heat exchanger, an effective fin model for the mixture of the storage and the fin materials was developed and implemented. The effective model was first adjusted and verified using detailed reference simulations of the discretized fin structure with ANSYS Fluent. Finally, simulations with the coupled large-scale models of two reference finned tube storage systems were performed: The first one used single-phase oil as heat transfer fluid and radially oriented plate fins in the storage material. The second one used a two-phase water/steam heat transfer fluid and axially extruded fins in the storage material. The effective fin model could be verified by comparison with detailed models of the same storage systems that discretized the fin structures. The proposed modelling approach proved to be accurate and enables a more efficient design and optimization process for latent thermal energy storage systems.

Keywords

Latent heat storage (LHS), phase change material (PCM), heat transfer fluid (HTF), solidification and melting, boiling and condensation, effective thermal conductivity

Highlights

- Coupled numerical modeling of heat transfer fluid, heat exchanger and phase change material
- Quasi-stationary modelling of heat transfer fluid verified with Apros® reference results
- Effective fin models calibrated and verified using discretized fin models in ANSYS® Fluent
- Efficient and verified modelling enables parameter and design studies of large scale LTES

---

[*] *Corresponding author e-mail address: julian.r.vogel@gmail.com, ORCID ID: https://orcid.org/0000-0001-9792-2332*

Nomenclature

Latin

A	area, $[A] = \mathrm{m}^2$
$A,\ B,\ C$	model parameters in frictional pressure drop model
$\boldsymbol{A}, \boldsymbol{B}$	system of equations matrices
a	coefficients of discretized equation
C_0	distribution coefficient in drift flux model
c	specific heat capacity, $[c] = \mathrm{J/(kg\,K)}$
D	diameter, $[D] = \mathrm{m}$
D_t	tube distance, $[D_t] = \mathrm{m}$
f	liquid phase fraction
G	mass flux, $[G] = \mathrm{kg/(s\,m^2)}$
g	gravity, $[g] = \mathrm{m/s^2}$
H	heat transfer coefficient, $[H] = \mathrm{W/(m^2\,K)}$
H	height, $[H] = \mathrm{m}$
h	specific enthalpy, $[h] = \mathrm{J/kg}$
j	volume flux in drift flux model, $[j] = \mathrm{m/s}$
k	thermal conductivity, $[k] = \mathrm{W/(m\,K)}$
L	latent heat, $[L] = \mathrm{kJ/kg}$
$\dot{m}$	mass flow rate, $[\dot{m}] = \mathrm{kg/s}$
Nu	Nußelt Number
N	number of time steps
$\boldsymbol{n}$	normal vector, $\boldsymbol{n} = (n_x, n_y, n_z)^\top$, $[\boldsymbol{n}] = \mathrm{m}$
P	factor of parallelism
p	pressure, $[p] = \mathrm{Pa}$
Pr	Prandtl Number
$\dot{Q}$	heat transfer rate, $[\dot{Q}] = \mathrm{W}$
q''	heat flux, $[q''] = \mathrm{W/m^2}$
R	radius, $[R] = \mathrm{m}$
R	thermal resistance, $[R] = \mathrm{K/W}$
r, φ	cylindrical coordinates, $[r] = \mathrm{m}$, $[\varphi] = \deg$
Re	Reynolds Number
S_h	source term in energy equation, $[S_h] = \mathrm{W/m^3}$
T	temperature, $[T] = \mathrm{°C}$
t	time, $[t] = \mathrm{s}$
$\boldsymbol{u}$	velocity vector, $\boldsymbol{u} = (u, v, w)^\top$
u, v, w	x-, y-, z-velocities, $[u, v, w] = \mathrm{m/s}$
v_{fin}	fin volume fraction
V	volume, $[V] = \mathrm{m^3}$
$V_{vap,j}$	drift velocity, $[V_{vap,j}] = \mathrm{m/s}$
x	steam quality
x, y, z	coordinates, $[x, y, z] = \mathrm{m}$

Greek

α	void fraction
β	underrelaxation factor
σ	surface tension, $[\sigma] = \mathrm{N/m}$
δ	condensation film thickness, $[\delta] = \mathrm{m}$
ζ	friction factor
η	dynamic viscosity, $[\eta] = \mathrm{Pa\,s}$
ν	kinematic viscosity, $[\nu] = \mathrm{m^2/s}$
ξ	transition range around melting point temperature
ρ	density, $[\rho] = \mathrm{kg/m^3}$
ϕ	inclination angle, $[\phi] = \deg$
ψ	smoothing function

Subscripts

0	initial value
A	due to acceleration
atm	atmospheric
B	boiling
b	boundary
C	condensation
E, e	east control volume node, face
Eff	effective
evap	evaporation
F	frictional
FC	forced convection
f	fluid
G	gravitational
H	homogeneous
I	momentum
lat	latent heat content
liq	liquid
Lo	liquid only
m	melting point
max	maximum
N, n	north control volume node, face
P	center control volume node
par	parallel
ref	reference
S, s	south control volume node, face
sat	saturation
sens	sensible heat content
ser	series
sol	solid
t	turbulent
vap	vapor
Vo	vapor only
W, w	west control volume node, face
w	wall

Superscripts

i, j, k	iteration indices
n	time step

Symbols

∇	nabla operator: $\nabla = \left(\frac{\partial}{\partial x}, \frac{\partial}{\partial y}, \frac{\partial}{\partial z}\right)$
Δ	finite difference
$\widetilde{\{\}}$	smoothened, underrelaxed or modified value

Abbreviations

1Ph	single-phase
2Ph	two-phase
AAS	"as a server"
DF	discretized fin
EF	effective fin
FV	finite volume
HEX	heat exchanger
HTF	heat transfer fluid
IF	interface
PCM	phase change material

1. Introduction

Climate change and its consequences have been becoming increasingly evident [1]. One of the most promising contributions to counteract climate change is the increased use of sustainable energy sources free of greenhouse gas emissions. The storage of thermal energy can play a critical role in improving the availability of fluctuating sustainable energy sources [2]. A goal with thermal energy storage is to make use of low cost and sustainable storage materials for implementing large storage capacities and supplying energy flexibly.

In a latent thermal energy storage (LTES), which utilizes the phase change on the storage material side, the latent heat of fusion stores large amounts of energy per unit volume in a narrow temperature range. Various concepts for storing thermal energy in phase change materials (PCMs) have been discussed in general by Cabeza [3]. The finned shell-and-tube storage concept has been investigated by several authors, including a clipped fin and a large-scale design by Laing et al. [4], an exterior clamped fin discussed by Walter et al. [5] and a large-scale design by Olcese et al. [6]. In each of these designs, the tubes were vertically oriented and the heat transfer fluid (HTF) inside the tubes was either a single-phase fluid, such as thermal oil, or a two-phase fluid, such as water/steam, which condensed during charging and evaporated during discharging. Application examples of these HTFs have been solar thermal power plants [7,8], or industrial processes [9].

The kind of PCM inside the storage shell was selected based on a range of criteria [10], including the melting temperature, which needs to be paired with the system into which the unit is being integrated. Many applicable storage materials have a low thermal conductivity. This especially limits heat transfer during solidification, when natural convection is not possible in the solid layer forming at the heat sink and heat transfer occurs only by heat conduction.
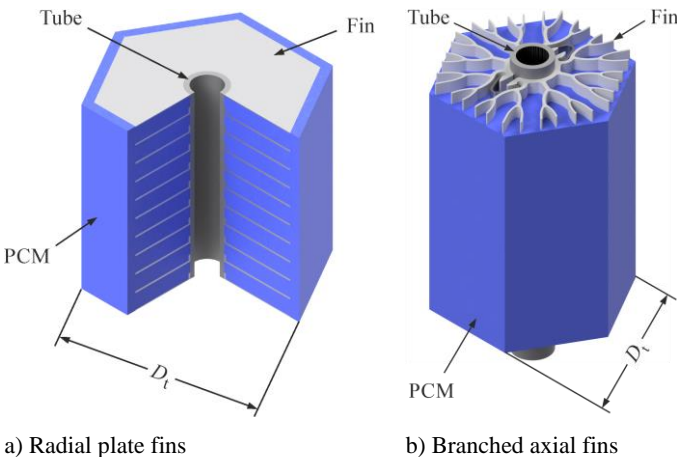

Figure 1: Two different heat exchanger (HEX) designs showing the tube, fins and surrounding PCM.

To overcome the low thermal conductivity of PCMs, one concept has been to increase the surface area of the heat exchanger (HEX), as discussed in the review papers by Jegadheeswaran and Pokehar [11], Agyenim et al. [12], Liu et al. [13] and Gasia et al. [14]. In a vertical shell-and-tube arrangement, the surface areas of the tubes have been extended with fins made of a highly thermally conductive material. Several designs of finned tubes have been examined, including a branched design by Walter et al. [5], a radial plate design by Laing et al. [8] and a different branched design by Johnson et al. [9]. The latter two designs, which were also applied throughout this work, are depicted in Figure 1.

For design and analysis work of latent heat storage systems, the storage system, or at least the complete finned tubes portion of the storage system, has to be modelled. The numerical representation must include a) modelling of the HTF region, b) modelling of the storage region containing the HEX and the PCM and c) coupling of the two regions.

The fluid flow and heat transfer in the HTF has been studied in many works regarding different applications. The understanding and modeling of two-phase flows including condensation and boiling has been deeply analyzed and well documented in literature, for example in the publications by Whalley [15], Ghiaasiaan [16], Baehr and Stephan [17] and in the VDI Heat Atlas [18]. Condensation can occur as film condensation or dropwise condensation [15]. If we do not design the system specifically for dropwise condensation, we can assume film condensation [18]. Boiling can occur as subcooled or saturated nucleate boiling, or as convective boiling [15]. When the critical heat flux is exceeded, dryout will occur at the tube wall [15]. Since the mass flux is usually low in latent heat storage systems, a so called hydrodynamic dryout will occur, where liquid is not entrained by the vapor flow but a horizontal surface between liquid and vapor forms, as explained by Sun et al. [19]. The two-phase flow in vertical latent thermal energy storage systems was specifically studied by Keller [20], who compiled and compared correlations for pressure drop and heat transfer and built a custom model for steady one-dimensional heterogeneous two-phase flow with boundary conditions of a LTES system. This model was extended and coupled to the storage region in the present study.

The HEX and PCM have been modeled together as a storage region. Johnson et al. [9] studied and compared three different HEX geometries during the design process of a LTES system. They analyzed the heat transfer in a two-dimensional horizontal cut of the storage region in a vertical finned tube arrangement, neglecting both the spatial and temporal variation of the HTF and natural convection in the PCM. Walter et al. [5] studied a small three-dimensional section of the storage region in a vertical finned tube design including natural convection. To analyze the impact of natural convection, Vogel and Johnson [21] studied the three-dimensional heat transfer in four different HEX geometries including the ones used in the present study. The results indicated that natural convection is weak in a HEX with narrow gaps between fins (assuming typical dimensions and boundary conditions of a LTES). In these cases, including the present study, natural convection may be neglected in good approximation. Vogel and Johnson [21] also indicated other simplifications: e.g. sinking of the solid phase (close-contact melting) had to be neglected due to high model complexity, see Kozak and Ziskind [22] for a recent model.

In all the beforementioned discretized fin (DF) models, the fins were discretized, which lead to accurate results but large model complexity. For efficient computation, Bauer [23] proposed an analytical model with mixed material properties for mixtures of PCM and fins. Meshgin and Xi [24] proposed effective thermal conductivity models for mixtures of PCM and

concrete. Tay et al. [25] introduced a weighted average between the effective thermal conductivities of serial and parallel arrangements of PCM and fins. However, to simulate arbitrary unstructured fin geometries, the available models had to be further extended for the present work.

To model an LTES on a system scale, the HTF region and the storage region (consisting of HEX and PCM) have to be coupled and transient simulations have to be performed. However, such models of finned tube LTES have been sparsely reported. Some models of shell-and-tube systems without fins and without two-phase HTF were compiled in the review by Verma et al. [26]. Another model including radial plate fins in the HEX, water as HTF and an organic material as PCM was developed by Kuboth et al. [27]. Their approach proved to be accurate, however, it did not include models for two-phase HTF or branched-fin geometries. Stueckle et al. [28] used Dymola to model a storage system including two-phase HTF flow of water in vertical tubes, a HEX using plate fins and a nitrate salt as the PCM. The model was further refined by Johnson et al. [9] to design a LTES system using branched axial fins in the HEX. While satisfactory results were achieved with this model, the computational representation was not flexible and efficient enough for parameter studies. In conclusion, many models have been developed for detailed parts of the storage system, namely the HTF region and the storage region of HEX and PCM. But computationally efficient storage system models coupling the HTF region and the storage region to obtain a realistic transient solution are rarely found.

In the present work, a model for large-scale industrial storage systems is proposed. The modelling approach consists of two parts: The model for the HTF region is described in section 2 and the model for the storage region (including PCM and HEX) is described in section 3. The effective fin (EF) model, which is a simplified representation of arbitrary fin geometries in the storage region, is proposed. The coupling of the HTF region and storage region models is described in section 4. The results and discussion are shown in section 5, which is divided into three parts: Firstly, the model of the HTF is analyzed by simulating test cases that include only the flow of the HTF in a vertical tube. The results are verified with reference simulations obtained using the commercial software Apros®. Secondly, the effective fin (EF) model is adjusted using another set of test cases that include different sections of storage regions (HEX+PCM). The results are compared and verified to discretized fin (DF) models implemented in MATLAB and ANSYS Fluent. Finally, the effective fin (EF) method is used in the coupled large-scale model to simulate a set of transient test cases including the HTF region and storage region. Simulations with the effective fin (EF) model are compared to simulations with the discretized fin (DF) model implemented in either ANSYS Fluent for the branched axial fin or MATLAB for the radial plate fin. This way, the accuracy of the effective fin (EF) model compared to the discretized fin (DF) model is highlighted. In the last section 6, conclusions and an outlook are given.

2. Numerical modeling of the heat transfer fluid

The heat transfer fluid that flows inside of the vertical tubes was either single-phase liquid thermal oil or two-phase liquid/vapor water. The operation mode is as follows: the HTF flows downwards during charging and upwards during discharging. Using a two-phase fluid, superheated vapor condensates to water during charging and subcooled liquid boils to vapor during discharging. The assumed two-phase fluid flow and heat transfer in a LTES system is illustrated in Figure 2.

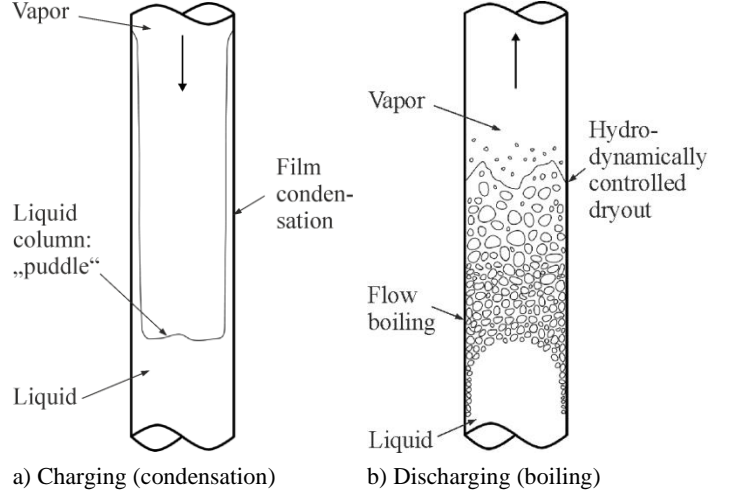a) Charging (condensation) b) Discharging (boiling)

Figure 2: Assumed flow of two-phase heat transfer fluids in vertical tubes of a LTES system during charging and discharging. [20]

Melting and solidification in latent heat storage are transient processes that usually take a few hours. In contrast, the time scales of the two-phase flow dynamics of the HTF in the vertical tubes are several orders of magnitude smaller and we can assume the flow to be quasi-stationary. Hence, we solved steady fluid flow and updated the solution constantly during the transient solid-liquid phase-change process of the PCM. Moreover, we do not necessarily need to resolve the state of the fluid over a radial coordinate inside the tube. Rather, we assumed a constant bulk state of the fluid and closed the governing equations with empirical pressure drop and heat transfer relations. Finally, we did not resolve the two phases separately. Instead, we used a heterogeneous two-phase model that regards the two phases as a mixture with a slip velocity between phases. We further assumed thermodynamic equilibrium. These simplifications led to an efficient one-dimensional model, that is suitable for modeling the HTF in LTES.

2.1. Material properties

The heat transfer fluid was either thermal oil or water. For the test case with thermal oil, Syltherm-800 from The Dow Chemical Company was used [29]. Example properties at distinct temperatures are given in Table 1.

Table 1: Example thermo-physical material properties of the thermal oil Syltherm-800.

	Unit	$T = 172\,°C$	$T = 222\,°C$	$T = 272\,°C$
ρ	$\dfrac{\text{kg}}{\text{m}^3}$	799.5	752.2	701.4
c	$\dfrac{\text{J}}{\text{kg K}}$	1868	1953	2039
k	$\dfrac{\text{W}}{\text{m K}}$	0.1064	0.09702	0.08761
μ	Pa s	0.001366	0.0008623	0.0005743

For water, the IAPWS-IF97 formulation [30,31] was used. Example properties at distinct temperatures are given in Table 2. The properties were calculated with the commercial library for MATLAB, FluidLAB LibIF97.

Table 2: Example thermo-physical material properties of water with IAPWS-IF97 formulation.

	Unit	Saturated liquid discharging $p = 81.1$ bar $T = 296\,°C$	Saturated steam charging $p = 106.984$ bar $T = 316\,°C$
ρ	$\dfrac{kg}{m^3}$	720.2	60.34
c	$\dfrac{J}{kg\,K}$	5640	7673
k	$\dfrac{W}{m\,K}$	0.5586	0.08243
μ	Pa s	0.00008737	0.00002051

2.2. Governing equations

The steady state mixture model is described by three conservation equations. The continuity equation states that the mass flux G is constant along the tube length (z-axis):

$$\frac{\partial G}{\partial z} = 0. \tag{1}$$

The momentum equation reduces to a pressure drop relation,

$$\frac{\partial p}{\partial z} = \left(\frac{\partial p}{\partial z}\right)_A + \left(\frac{\partial p}{\partial z}\right)_G + \left(\frac{\partial p}{\partial z}\right)_F, \tag{2}$$

consisting of parts due to acceleration (A), gravity (G) and friction (F). The first part due to acceleration is

$$\left(\frac{\partial p}{\partial z}\right)_A = -\frac{\partial}{\partial z}\left(\frac{G^2}{\rho_I}\right), \tag{3}$$

where ρ_I is the momentum density. The latter is calculated from the liquid and vapor densities, the steam quality x and the void fraction α of a two-phase mixture as described by Ghiaasiaan [16]:

$$\rho_I = \frac{1}{\left(\dfrac{x^2}{\rho_{vap}\alpha} + \dfrac{(1-x)^2}{\rho_{liq}(1-\alpha)}\right)}. \tag{4}$$

The second part due to gravity is

$$\left(\frac{\partial p}{\partial z}\right)_G = -g\rho_H, \tag{5}$$

where ρ_H is the homogeneous density:

$$\rho_H = \alpha\rho_{vap} + (1-\alpha)\rho_{liq}. \tag{6}$$

The frictional pressure drop is obtained from a constitutive equation given in section 2.3.2.

Finally, the energy equation is

$$G\frac{\partial h}{\partial z} = \frac{q_w'' A_w}{V}. \tag{7}$$

On the left-hand side is a convective term for the conservation of enthalpy. On the right-hand side is a volumetric heat flow rate source term, where q_w'' is the heat flux and A_w is the cylindrical wall surface area through which the heat is transferred.

The equilibrium steam quality was determined from the calculated enthalpies and the saturated liquid and vapor enthalpies obtained from the material property library:

$$x = \frac{h - h_{sat,liq}}{h_{sat,vap} - h_{sat,liq}}. \tag{8}$$

2.3. Constitutive equations

The constitutive equations are empirical relations that model physical phenomena not directly included in the governing equations and are needed to close the system of equations.

2.3.1. Void fraction

To calculate the void fraction α for the homogeneous model in the case of boiling, an exact relation is available:

$$\alpha_H = \left(1 + \frac{1-x}{x}\frac{\rho_{vap}}{\rho_{liq}}\right)^{-1}. \tag{9}$$

For the heterogeneous model in the case of boiling, the drift flux equation is used to modify the homogeneous void fraction:

$$\alpha = \frac{\alpha_H}{C_0 + \dfrac{V_{vap,j}}{j}}, \tag{10}$$

where C_0 is the distribution coefficient, $V_{vap,j}$ is the drift velocity and j is the volume flux. Woldesemayat and Ghajar [32] provide values for C_0 and $V_{vap,j}$ of a modified Dix drift flux correlation:

$$
\begin{aligned}
C_0 &= \frac{j_{vap}}{j}\left[1 + \left(\frac{j}{j_{vap}} - 1\right)^{\left(\frac{\rho_{vap}}{\rho_{liq}}\right)^{0.1}}\right], \\
V_{vap,j} &= 2.9\left[\frac{gD\sigma(1 + \cos\phi)(\rho_{liq} - \rho_{vap})}{\rho_{liq}^2}\right](1.22 \\
&\quad + 1.22\sin\phi)^{\frac{p_{atm}}{p}}.
\end{aligned} \tag{11}
$$

To calculate the void fraction α in the case of condensation, a custom approach by Keller [20], which derives the void fraction from the condensation film thickness δ, was used:

$$\alpha = \left(1 - \frac{2\delta}{D}\right)^2 \tag{12}$$

The film thickness δ depends on the film length Δz_{film} and is calculated from the Nusselt theory, which can be found in the book by Ghiaasiaan [16] (p. 443):

$$\delta(\Delta z_{film}) = \left(\frac{4\eta_{liq}\lambda_{liq}(T_{sat} - T_w)}{gh_{evap}\rho_{liq}(\rho_{liq} - \rho_{vap})}\Delta z_{film}\right)^{\frac{1}{4}}. \tag{13}$$

2.3.2. Frictional pressure drop

For single-phase flow, which means either vapor or liquid, the frictional pressure drop was calculated from the Darcy-Weisbach equation [18]:

$$\left(\frac{\partial p}{\partial z}\right)_{\text{F,1Ph}} = -\frac{\zeta}{D}\frac{\rho u^2}{2} = -\frac{\zeta}{D}\frac{G^2}{2\rho}. \quad (14)$$

The friction factor ζ depends on the wall roughness and the Reynolds number of the flow

$$Re_D = \frac{GD}{\eta}. \quad (15)$$

The friction factor $\zeta(Re_D)$ was calculated using multiple correlations by Stokes, Blasius, Konakov, Filonenko, and Prandtl & Kármán, which are compiled in the VDI Heat Atlas [18]. These correlations are vaild for smooth tube walls or small wall roughness and a certain Reynolds number range. Multiple correlations were used to cover a large Reynolds number range. Correlations for rough tube walls are also available in the VDI Heat Atlas [18].

To calculate the pressure drop in two-phase flow regions, a heterogeneous model was used. Many available correlations were compiled by Xu et al. [33]. Keller [20] tested and compared the most promising correlations from Friedel [34] and Müller-Steinhagen and Heck [35] for latent heat storage test cases and found that the results from both models were similar. However, the pressure drop was dominated by the gravitational part and the frictional pressure drop was negligible in these cases. For the present model, the correlation by Müller-Steinhagen and Heck [35] was used,

$$\left(\frac{\partial p}{\partial z}\right)_{\text{F,2Ph}} = C_1(1-x)^{\frac{1}{C_2}} + Bx^{C_2}, \quad (16)$$

for which the following constants are needed:

$$
\begin{aligned}
C_1 &= A + 2(B-A)x, \\
C_2 &= 3, \\
A &= \left(\frac{\partial p}{\partial z}\right)_{\text{F,1Ph,liq}} = \zeta_{\text{Lo}}\frac{1}{D}\frac{G^2}{2\rho_{\text{liq}}}, \\
B &= \left(\frac{\partial p}{\partial z}\right)_{\text{F,1Ph,vap}} = \zeta_{\text{Vo}}\frac{1}{D}\frac{G^2}{2\rho_{\text{vap}}}.
\end{aligned} \quad (17)
$$

The two-phase friction factor for only the liquid phase ζ_{Lo} and that for only the vapor phase ζ_{Vo} were calculated as the single-phase friction factors. The Reynolds numbers were calculated as if only liquid or only vapor would flow through the tube:

$$
\begin{aligned}
Re_{D,\text{Lo}} &= \frac{GD}{\eta_{\text{liq}}}, \\
Re_{D,\text{Vo}} &= \frac{GD}{\eta_{\text{vap}}}.
\end{aligned} \quad (18)
$$

However, Müller-Steinhagen used the single-phase friction factor correlations by Stokes and Blasius in the following regions:

$$\zeta = \begin{cases} \dfrac{64}{Re_D} & \text{for } Re_D \le 1187 \\[2mm] \dfrac{0.3164}{\sqrt[4]{Re_D}} & \text{for } Re_D > 1187 \end{cases} \quad (19)$$

2.3.3. Heat flux

The heat flux is generally composed of a single-phase forced convection term q_{FC}'', a two-phase boiling term q_{B}'' and a two-phase condensation term q_{C}'':

$$q'' = q_{\text{FC}}'' + q_{\text{B}}'' + q_{\text{C}}''. \quad (20)$$

If boiling occurs, the heat flux in the boiling region is calculated as a superposition of the forced convection term evaluated in the boiling region and the boiling term: $q'' = q_{\text{FC}}'' + q_{\text{B}}''$. This superposition was similarly introduced by the Chen correlation for flow boiling described by Ghiaasiaan [16]. However, the original Chen correlation is used here in a simplified form as described by Keller [20]. In the boiling region, the condensation term is $q_{\text{C}}'' = 0$. Analogously, if condensation occurs, the heat flux in the condensation region is calculated as a superposition of the forced convection term evaluated in the condensation region and the condensation term, $q'' = q_{\text{FC}}'' + q_{\text{C}}''$, while the boiling term is $q_{\text{B}}'' = 0$. If neither boiling nor condensation occurs, the boiling and convection terms are $q_{\text{B}}'' = q_{\text{C}}'' = 0$ and heat flux occurs by forced convection, $q'' = q_{\text{FC}}''$.

Boiling heat flux will occur if $T_{\text{w}} \ge T_{\text{sat}}$ and $x < 1$. Condensation heat flux will occur if $T_{\text{w}} \le T_{\text{sat}}$ and $x > 0$. In both cases, two regions are distinguished: the first region is the subcooled region ($x \le 0$) for boiling or the superheated region ($x \ge 1$) for condensation. In these cases, the heat flux is calculated with the driving temperature difference to the saturation temperature T_{sat}:

$$
\begin{aligned}
q_{\text{B,x}\le 0}'' &= H_{\text{B}}(T_{\text{w}} - T_{\text{sat}}), \\
q_{\text{C,x}\ge 1}'' &= H_{\text{C}}(T_{\text{w}} - T_{\text{sat}}).
\end{aligned} \quad (21)
$$

The second region is the saturated region ($0 < x < 1$), where the heat flux is calculated using the driving temperature difference to the mean fluid temperature T:

$$
\begin{aligned}
q_{\text{B,}0<x<1}'' &= H_{\text{B}}(T_{\text{w}} - T), \\
q_{\text{C,}0<x<1}'' &= H_{\text{C}}(T_{\text{w}} - T)
\end{aligned} \quad (22)
$$

The forced convection heat flux is calculated with a forced convection heat transfer coefficient H_{FC} and the temperature difference between the wall T_{w} and the mean fluid temperature T:

$$q_{\text{FC}}'' = H_{\text{FC}}(T_{\text{w}} - T). \quad (23)$$

The forced convection heat transfer coefficient is calculated with properties of the liquid phase in the single-phase liquid region, with properties of the vapor phase in the single-phase vapor region, or with mixture properties in the two-phase boiling or condensation regions. The correlations for boiling heat transfer coefficients usually use the liquid phase properties for the forced convection term. And, the forced convection term is commonly neglected in the condensation heat transfer correlations. However, using the forced convection term with mixture properties in two-phase regions greatly improves convergence of the iterative solution procedure. The reason for this is that a smooth transition for the forced convection term between the two-phase and the single-phase regions is automatically established, and no discontinuity occurs.

6

2.3.4. Forced convection heat transfer coefficient

The forced convection heat transfer coefficient is calculated using the Dittus-Boelter correlation for turbulent flow [36]:

$$Nu_t = 0.023 Re^{0.8} Pr^n. \tag{24}$$

The value n is different for heating ($n = 0.4$) and cooling ($n = 0.3$). The correlation is only valid for turbulent flow with $Re > 10000$ in smooth tubes. To approximately include the laminar case, the Nusselt number was restricted [37]:

$$Nu = \max(Nu_t, 3.66). \tag{25}$$

The heat transfer coefficient was then calculated with the thermal conductivity k of the liquid or vapor phase and the diameter D:

$$H_{FC} = \frac{k}{D} Nu. \tag{26}$$

2.3.5. Boiling and condensation heat transfer coefficients

There is a vast amount of different correlations for the boiling heat transfer coefficient H_B and the condensation heat transfer coefficient H_C. Many of the correlations were compiled by Ghiaasiaan [16], Baehr and Stephan [17] and the VDI Heat Atlas [18]. For verification of the HTF model of the present work, the nucleate boiling correlation by Thom [37],

$$H_B = 1971.2 \exp\left(\frac{2p}{8687000}\right)(T_w - T_{sat}), \tag{27}$$

was used.

For condensation, the film condensation correlation by Chen et al. [38] was used,

$$H_C = \frac{k_{liq}}{\left(v_{liq}{}^2/g\right)^{\frac{1}{3}}} \left[\left(0.312 Re_{liq}^{-1.32} + \frac{Re_{liq}^{2.4} Pr_{liq}^{3.9}}{2.37 \cdot 10^{14}} \right)^{\frac{1}{3}} \right.$$
$$\left. + \frac{A_D Pr_{liq}^{1.3}}{771.6} \left(Re_{Lo} - Re_{liq} \right)^{1.4} Re_{liq}^{0.4} \right]^{0.5},$$
$$A_D = \frac{0.252 \eta_{liq}^{1.177} \eta_{vap}^{0.156}}{D^2 g^{\frac{2}{3}} \rho_{liq}^{0.553} \rho_{vap}^{0.78}},$$
$$Re_{liq} = \frac{(1 - \tilde{x})|G|D}{\eta_{liq}},$$
$$\tilde{x} = \begin{cases} x & \text{for } x < 0.99 \\ 0.99 & \text{for } x \geq 0.99 \end{cases}, \tag{28}$$

where the steam quality was restricted, as a value of $\tilde{x} = 1$ would lead to a singularity in the correlation.

With these correlations satisfying results were obtained, which are shown in section 5.1 on the verification of the HTF model. However, other boundary conditions may lead to different mechanisms of the two-phase flow and other correlations may be necessary. For example, the critical heat flux may be reached during boiling, which can be checked for water with the data table by Groeneveld [39].

The discontinuities between a region of high boiling or condensation heat transfer coefficient H_B or H_C and a region of low single-phase forced convection heat transfer coefficient H_{FC} above or below were additionally smoothened to signifi-

cantly improve convergence of the iterative solution procedure. During subcooled boiling, there is a naturally smooth transition from forced convection in the liquid to nucleate boiling. Similarly, during superheated condensation, there is a smooth transition from forced convection in the vapor into film condensation. However, there is no transition yet at the hydrodynamically controlled dryout during boiling or at the formation of a water column, we call it puddle, during condensation. These points are indicated in Figure 2. For simplicity and improved convergence, we did not introduce additional correlations at this point. Instead, we introduced linear transition functions only in a small region near the discontinuities. The smoothing functions are defined as:

$$\psi_{dryout} = \begin{cases} 0 & \text{for } x < x_{dryout} \\ \dfrac{x - x_{dryout}}{1 - x_{dryout}} & \text{for } x \geq x_{dryout} \end{cases},$$
$$\psi_{puddle} = \begin{cases} 0 & \text{for } x > x_{puddle} \\ \dfrac{x_{puddle} - x}{x_{puddle}} & \text{for } x \leq x_{puddle} \end{cases}. \tag{29}$$

The smoothened heat transfer coefficients are then calculated as follows:

$$\tilde{H}_B = (1 - \psi_{dryout}) H_B$$
$$\tilde{H}_C = (1 - \psi_{puddle}) H_C \tag{30}$$

We chose values of $x_{dryout} = 0.9$ and $x_{puddle} = 0.1$ for this study, but values closer to 1 or 0 are also feasible, when the computational mesh is sufficiently fine or the discontinuity is small.

For use in the coupled model, we generally found that the best trade-off between accuracy and simplicity was to use constant values for the boiling and condensation heat transfer coefficients H_B and H_C and neglect the slight variation over the length of the two-phase region. Therefore, in a first step, the boiling and condensation heat transfer coefficients have to be calculated over the two-phase region of the tube length. Then, the boiling and condensation heat transfer coefficients have to be averaged over the boiling or condensation region. Finally, the constant averaged values H_B or H_C can be used in the simulation. This leaded to an efficient and stable solution convergence for many quasi-steady time steps.

2.4. Discretization

The governing equations (2) and (7) were discretized using a one-dimensional finite volume mesh. The pressures and enthalpies were solved on the control volume faces and then linearly interpolated on the control volume nodes, where material properties and other quantities were defined. The control volume faces and nodes are shown in Figure 3.
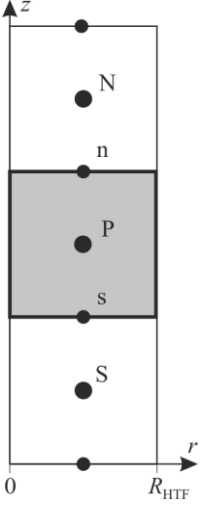
Figure 3: Discretization of the HTF model on control volume faces s, p, n and interpolation of the solution on control volume nodes S, P, N.

The governing equations were solved in a segregated fashion, because they are only coupled via the material properties. For a two-phase fluid, the material properties are strongly nonlinear, and several iterations of the governing equations were required to resolve the coupling. The new values at iteration $j + 1$ were calculated from the values of the last iteration j.

The pressures at the control volume faces were obtained from the discretized momentum equation:

$$p_n^{j+1} - p_s^{j+1} = \left[\text{sign}(G) \cdot \left(\left(\frac{\partial p}{\partial z}\right)_A + \left(\frac{\partial p}{\partial z}\right)_F \right) + \left(\frac{\partial p}{\partial z}\right)_G \right]_P^j \Delta z.$$
(31)

As the pressure gradients due to acceleration and friction depend on the flow direction, the sign of the mass flux was used to obtain a universal formulation for upward flow during discharging and downward flow during charging.

The enthalpies at the control volume faces were obtained from the discretized energy equation:

$$h_n^{j+1} - h_s^{j+1} = \frac{1}{G} \left[\frac{q_w'' A_w}{V} \right]_P^j \Delta z.$$
(32)

It is also valid for both upward and downward flow as long as the mass flux G is inserted with the appropriate sign.

At the inlet boundary, which is the uppermost node during charging and the lowermost node during discharging, the pressure and enthalpy are set to the inlet values:

$$p_b = p_{\text{Inlet}}, \qquad h_b = h_{\text{Inlet}}.$$
(33)

2.5. Solution procedure

The discretized governing equations (31) and (32) could be solved explicitly, but it was convenient to write linear systems, because the flow direction and boundary conditions were then automatically resolved. The resulting linear systems for pressure

$$A_p \cdot p^{j+1} = B_p^j,$$
(34)

and enthalpy

$$A_h \cdot h^{j+1} = B_h^j$$
(35)

were solved in MATLAB with the function mldivide (invoked with the backslash operator).

The solution procedure for one iteration was as follows: At first, the heat transfer coefficients (26) and (30), and the heat flux (20) were calculated. After that, the pressures were obtained by solving the linear system (34). Then, the linear system for enthalpies (35) was solved, and the steam quality (8) and the void fraction (10) or (12) were calculated. Finally, material properties and derived variables, such as dimensionless quantities, were calculated.

To stabilize and speed up solution convergence, underrelaxation of the heat flux and enthalpy was used:

$$\tilde{q}_w''^{j+1} = \beta_q q_w''^{j+1} + \left(1 - \beta_q\right) q_w''^{j},$$
$$\tilde{h}^{j+1} = \beta_h h^{j+1} + (1 - \beta_h) h^{j+1}.$$
(36)

For two-phase flow of water, an underrelaxation factor for heat flux $\beta_q = 0.9$ and enthalpy $\beta_h = 0.6$ led to stable and fast convergence. For single-phase flow of thermal oil, only slight underrelaxation of the enthalpy was used with $\beta_h = 0.8$.

The solution procedure was repeated until convergence was reached with the following criterion, which states that the L^2 norm of the relative change of wall heat flux from the last to the current iteration must fall below 10^{-3}:

$$\left\| \frac{q_w''^{j+1} - q_w''^{j}}{q_w''^{j+1}} \right\|_2 < 10^{-3}.$$
(37)

On average, 4 iterations were needed for calculating the solution of the single-phase HTF thermal oil and 6 iterations were needed for the solution of the two-phase HTF water.

3. Numerical modeling of the storage material and the heat exchanger

The HEX in the storage region consists of a vertical tube with either radial plate fins or branched axial fins, as shown in Figure 1. Different models were used in this study: a detailed representation with discretized fins (DF) of both fin types was used as reference. For the branched axial fin, a model for unstructured geometries, which allows for arbitrary shapes of the tube, fin and PCM volumes was used. As a reference for the radial plate fins, a model for structured cylindrical geometries was used. Both models resolve the detailed fin structure. To reduce the complexity and computational effort, an effective fin (EF) model was developed and used in the model for cylindrical geometries. The effective fin model can approximately represent either of the fin geometries on a structured cylindrical grid. This section is structured as follows: first, material properties of the storage region are presented. Then, the DF model for unstructured geometries implemented with ANSYS Fluent is summarized. Finally, the model for structured cylindrical geometries, which includes the EF model and was implemented with MATLAB, is derived.

3.1. Material properties

Two different PCMs were used in the present study: the first was the eutectic mixture of potassium nitrate and sodium nitrate (KNO3-NaNO3) and the second was sodium nitrate (NaNO3). The material properties were analyzed by Bauer et al. [40]. The fin material was aluminum 6060 and the tube material was steel 1.5415. It should be noted that nitrate salts are corrosive to these metals. However, we chose combinations that showed little corrosion in tests and therefore corrosive effects are not included in our models. The material properties of these PCMs and solid materials are given in Table 3.

Table 3: Thermo-physical material properties of PCMs (KNO3-NaNO3, NaNO3) [40], fin (Al 6060) and tube (St 1.5415).

Material property	Unit	KNO3-NaNO3	NaNO3	Fin Al 6060	Tube St 1.5415
ρ_{sol}	kg	2050.5	2113	2700	7850
ρ_{liq}	$\overline{m^3}$	1959	1908	-	-
c_{sol}	J	1350	1655	1020	482
c_{liq}	$\overline{kg\,K}$	1492	1655	-	-
k_{sol}	W	0.435	0.6	210	42.5
k_{liq}	$\overline{m\,K}$	0.457	0.514	-	-
T_m	°C	222	306	-	-
L	$\dfrac{kJ}{kg}$	108	178	-	-

The properties of the PCM in the solid and liquid state were assumed at temperatures close to the melting point T_m. The dependency on temperature was neglected, since phase change was the governing mechanism and the temperature did not depart significantly from the melting point throughout most of the phase change processes. However, when the sensible heating of the solid or liquid phase becomes significant, temperature dependency of the material properties should be considered. During phase change, the properties depended on the phase state, i.e. the liquid phase fraction f, which is introduced in the next section. The density was assumed to have the value of the liquid state, since the density cannot change without volume expansion and fluid flow. However, to include the effect of density change, the thermal conductivity and the heat capacity were adjusted with the density ratio between solid and liquid. We can then think of the material as being filled into the domain in the liquid form and during solidification, the material becomes a porous medium with mixture properties. The properties are defined as follows:

$$
\begin{aligned}
\rho &= \rho_{liq}, \\
c &= f c_{liq} + (1 - f)\frac{\rho_{sol}}{\rho_{liq}} c_{sol}, \\
k &= f k_{liq} + (1 - f)\frac{\rho_{sol}}{\rho_{liq}} k_{sol}.
\end{aligned}
\tag{38}
$$

It is worthwhile to note that the resulting thermal diffusivity is the same as with a variable density between liquid and solid. However, an increasing density with a constant volume during solidification would result in an unphysical mass gain, which would induce an increase of absolute latent and sensible energy capacity of the material. The formulation of equation (38) is an approximation that conserves mass and energy.

3.2. Model for unstructured geometries

The model for unstructured geometries was used to discretize the branched axial fin geometry, see Figure 1 b). The geometry including the tube, the PCM and the HEX is illustrated in Figure 4 a). The discretization on an unstructured finite volume mesh using ANSYS Fluent is shown in Figure 4 b).
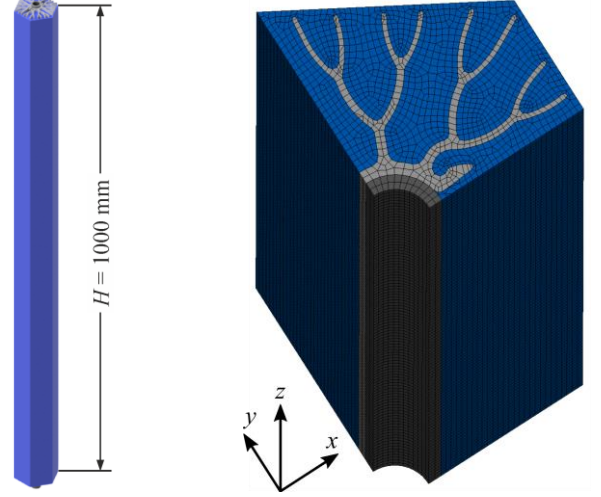
a) Geometry of tube, HEX and PCM with 1 m height. b) Discretization of a quarter section with 1 m height.

Figure 4: Geometry and discretization of a shell-and-tube storage system with the model for unstructured geometries.

3.2.1. Governing equations

The energy equation for the specific enthalpy h with a boundary source term S_b acting on a volume V and a source term for phase change S_f is

$$
\rho \frac{\partial h}{\partial t} - \nabla \cdot (k\nabla T) = \frac{S_b}{V} + S_f.
\tag{39}
$$

The energy equation was transformed with the enthalpy-porosity method [41–43]. The central idea of the method is to write the enthalpy h as the sum of the sensible enthalpy h_{sens} and the latent enthalpy h_{lat}:

$$
h = h_{sens} + h_{lat}.
\tag{40}
$$

The sensible enthalpy is

$$
h_{sens}(T) = \int_{T_{ref}}^{T} c_p \, dT'
\tag{41}
$$

and the latent enthalpy is the product of the latent heat of fusion L and the liquid phase fraction f:

$$
h_{lat} = Lf.
\tag{42}
$$

After introducing equation (40) in equation (39) and dropping the subscript sens, the phase change source term is found:

$$
S_f = -\rho L \frac{\partial f}{\partial t}.
\tag{43}
$$

The liquid phase fraction is in general defined by the temperature T in relation to the solidus temperature T_{sol} and the liquidus temperature T_{liq}:

$$f = \begin{cases} 0, & T \leq T_{\text{sol}} \\ 0 \dots 1, & T_{\text{sol}} < T < T_{\text{liq}} \\ 1, & T \geq T_{\text{liq}} \end{cases} \quad (44)$$

In the so-called mushy region, $0 < f < 1$, the material is neither solid nor liquid, but in a state of melting or solidification. In this region, a relationship between liquid phase fraction and temperature has to be defined. In this case, a linear relationship over a small temperature range of 2ξ between $T_{\text{sol}} = T_{\text{m}} - \xi$ and $T_{\text{liq}} = T_{\text{m}} + \xi$ is introduced and the liquid phase fraction is then defined as:

$$f = \begin{cases} 0, & T \leq T_{\text{m}} - \xi \\ \dfrac{T - (T_{\text{m}} - \xi)}{2\xi}, & T_{\text{m}} - \xi < T < T_{\text{m}} + \xi \\ 1, & T \geq T_{\text{m}} + \xi \end{cases} \quad (45)$$

3.2.2. Discretization

For this large geometry, a coarse mesh was generated in ANSYS meshing [44]. The mesh consisted of 134,300 Prism and Hexahedron cells with an element size in the radial direction in the range of 0.5…1 mm and a transition rate of 1.5. The element size in the axial direction had a fixed value of 10 mm. The time step was set to 10 s and the scaled residual convergence criterion for the energy equation was set to 10^{-8}.

The governing equations were discretized with implicit time integration in ANSYS Fluent 16 [44]. The second-order derivatives in the diffusive terms were approximated by second-order central differences. The resulting linear system was solved with an iterative method with algebraic multigrid acceleration [45].

3.3. Model for structured cylindrical geometries

The model for structured cylindrical geometries was used to discretize the radial plate fins, see Figure 1 a). The geometry, including the tube, the PCM and the HEX is illustrated in Figure 5 a). The discretization on a cylindrical mesh using the MATLAB computer program is shown in Figure 5 b).
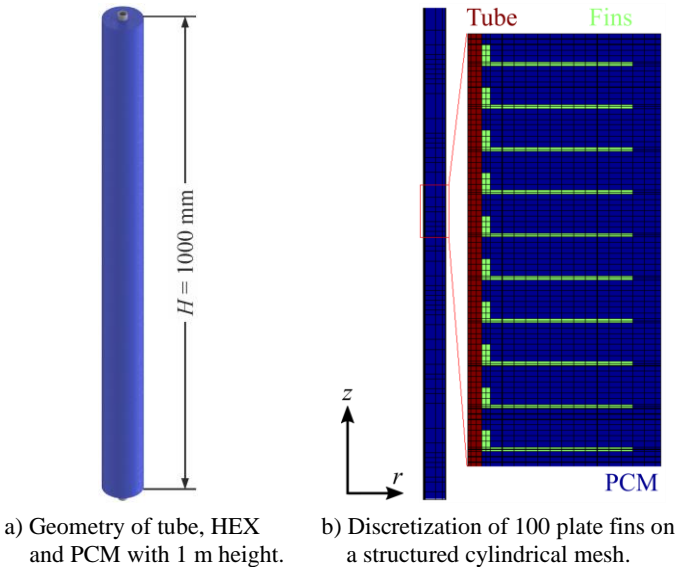

a) Geometry of tube, HEX and PCM with 1 m height.

b) Discretization of 100 plate fins on a structured cylindrical mesh.

Figure 5: Geometry and discretization of a shell-and-tube storage system with the model for structured cylindrical geometries.

3.3.1. Governing equations

The energy equation was transformed with the source term enthalpy method [43], comparable to the method in the ANSYS Fluent model. However, the energy equation (39) was directly formulated for the temperature T:

$$\rho c \frac{\partial T}{\partial t} - \nabla \cdot (k\nabla T) = \frac{S_{\text{b}}}{V} - \rho L \frac{\partial f}{\partial t}. \quad (46)$$

For the phase change process, a relationship between the liquid fraction f and the temperature T had to be defined. A straightforward approach was the linear relationship:

$$f = F(T) = \frac{T - T_{\text{sol}}}{T_{\text{liq}} - T_{\text{sol}}}, \quad (47)$$

where T_{liq} is the liquidus and T_{sol} is the solidus temperature, respectively. The values were chosen depending on a small number $\xi = 0.01$: $T_{\text{sol}} = T_{\text{m}} - \xi$ and $T_{\text{liq}} = T_{\text{m}} + \xi$.

3.3.2. Discretization

The governing equations were discretized on a structured finite volume mesh [46]. A control volume and its adjacent neighbor volumes are illustrated in Figure 6.
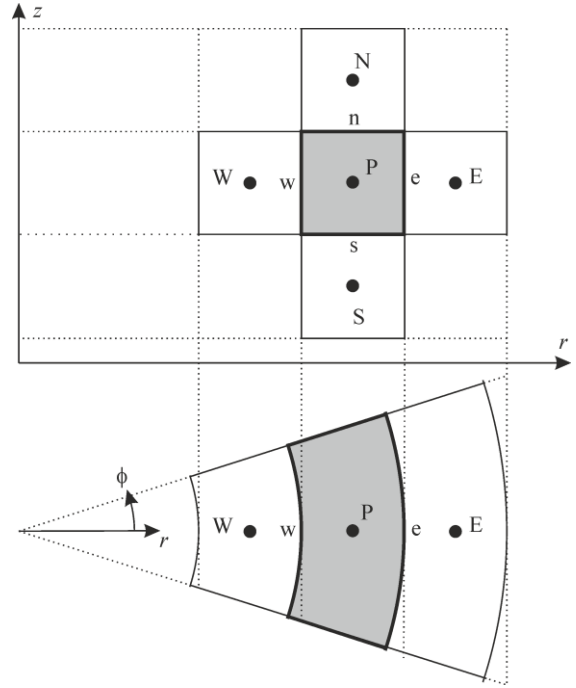

Figure 6: Illustration of a control volume with adjacent neighbors in cylindrical coordinates.

Equation (46) was integrated over a control volume V. Then, Gauss's theorem was applied to the diffusive term, which transforms the volume integral of the divergence of a quantity to a surface integral of the quantity projected to a normal vector n over the area A. The conservation equation in integral form is then:

$$\int_V \rho c \frac{\partial T}{\partial t} \, \mathrm{d}V - \int_A (k\nabla T \cdot n)\mathrm{d}A = S_{\text{b}} - \int_V \rho L \frac{\partial f}{\partial t} \, \mathrm{d}V. \quad (48)$$

Applying a second-order central finite difference approximation to the gradient in the diffusive term and assuming con-

stant values over the control volume, this equation was discretized to

$$\rho_P c_P V_P \frac{\partial T_P}{\partial t} - \left(\frac{T_E - T_P}{R_e} + \frac{T_W - T_P}{R_w} + \frac{T_N - T_P}{R_n} + \frac{T_S - T_P}{R_s} \right) = S_b - \rho_P L_P V_P \frac{\partial f_P}{\partial t}, \tag{49}$$

with the thermal resistances, R_w at the west face w, R_e at the east face e, R_n at the north face n and R_s at the south face s. The thermal resistances at the north and south faces were:

$$R_n = \frac{1}{A_n} \left(\frac{z_N - z_n}{k_N} + \frac{z_n - z_P}{k_P} \right),$$
$$R_s = \frac{1}{A_s} \left(\frac{z_S - z_s}{k_S} + \frac{z_s - z_P}{k_P} \right). \tag{50}$$

Due to cylindrical coordinates, the thermal resistances at the east and west faces were differently calculated:

$$R_e = \frac{1}{\Delta z \Delta \varphi} \left(\frac{\ln \frac{r_E}{r_e}}{k_E} + \frac{\ln \frac{r_e}{r_P}}{k_P} \right),$$
$$R_w = \frac{1}{\Delta z \Delta \varphi} \left(\frac{\ln \frac{r_P}{r_w}}{k_P} + \frac{\ln \frac{r_w}{r_W}}{k_W} \right). \tag{51}$$

This discretization with the lever rule considers that different control volumes may have different thermal conductivities as well as different sizes.

Applying a fully implicit time integration on equation (49) and rearranging, the discretized equation was:

$$\rho_P c_P V_P T_P^{n+1} - \Delta t \left(\frac{T_E^{n+1} - T_P^{n+1}}{R_e} + \frac{T_W^{n+1} - T_P^{n+1}}{R_w} + \frac{T_N^{n+1} - T_P^{n+1}}{R_n} + \frac{T_S^{n+1} - T_P^{n+1}}{R_s} \right)$$
$$= \rho_P c_P V_P T_P^n + \Delta t S_b^{n+1}$$
$$- \rho_P L_P V_P (f_P^{n+1} - f_P^n). \tag{52}$$

Introducing the coefficients

$$a_n = \frac{\Delta t}{R_n}, \qquad a_s = \frac{\Delta t}{R_s}, \qquad a_e = \frac{\Delta t}{R_e}, \qquad a_w = \frac{\Delta t}{R_w},$$
$$a_P = \rho_P c_P V_P + a_n + a_s + a_e + a_w, \tag{53}$$

the equation reads:

$$a_P T_P^{n+1} - a_n T_N^{n+1} - a_s T_S^{n+1} - a_e T_E^{n+1} - a_w T_W^{n+1}$$
$$= \rho_P c_P V_P T_P^n + \Delta t S_b^{n+1}$$
$$- \rho_P L_P V_P (f_P^{n+1} - f_P^n), \tag{54}$$

This system of equations formed a sparse pentadiagonal-matrix that was solved with a direct line-by-line TDMA (tridiagonal matrix algorithm) solver. The derivation is similar for one or three dimensions, where a tridiagonal- or septadiagonal matrix is formed, respectively.

Since the source term method introduced a second variable f, there were two variables f and T in one equation. The solution was to solve the equation iteratively and use a predictive equation for the liquid phase fraction f. For an iterative solution, the time step $n + 1$ was substituted with an iteration step $k + 1$ in equation (54) as proposed by Voller [43]:

$$a_P T_P^{k+1} - a_n T_N^{k+1} - a_s T_S^{k+1} - a_e T_E^{k+1} - a_w T_W^{k+1}$$
$$= \rho_P c_P V_P T_P^n + \Delta t S_b^{k+1}$$
$$- \rho_P L_P V_P (f_P^{k+1} - f_P^n). \tag{55}$$

The source term due to phase change was then:

$$S_f = -\rho_P L_P V_P (f_P^{k+1} - f_P^n). \tag{56}$$

For a proper implementation, this source term should be linearized. A linearization was explained in detail by Voller and Swaminathan [43], where f_P^{k+1} was represented by the following truncated Taylor series expansion:

$$f_P^{k+1} = f_P^k + \frac{\partial F(T)}{\partial T} \left(T_P^{k+1} - F^{-1}(f_P^k) \right). \tag{57}$$

At this point, the inverse and the derivative of the liquid phase fraction relationship (47) were needed:

$$F^{-1}(f_P^k) = (T_{liq} - T_{sol}) f_P^k + T_{sol}$$
$$\frac{\partial F(T)}{\partial T} = \frac{1}{T_{liq} - T_{sol}}. \tag{58}$$

Introducing equation (57) in equation (56), the source term could be written as:

$$S_f = S_{f,P} T_P^{k+1} + S_{f,C}. \tag{59}$$

with a temperature dependent part

$$S_{f,P} = -\rho_P L_P V_P \frac{\partial F(T)}{\partial T} \tag{60}$$

and a constant part

$$S_{f,C} = \rho_P L_P V_P \left(\frac{\partial F(T)}{\partial T} F^{-1}(f_P^k) - (f_P^k - f_P^n) \right). \tag{61}$$

The resulting evolution equation for the temperature was:

$$(a_P - S_{f,P}) T_P^{k+1} - a_n T_N^{k+1} - a_s T_S^{k+1} - a_e T_E^{k+1}$$
$$- a_w T_W^{k+1}$$
$$= \rho_P c_P V_P T_P^n + \Delta t S_b^{k+1} + S_{f,C}. \tag{62}$$

Now, the energy equation (62) could be solved to obtain the temperature at the new iterative level T^{k+1} from the temperature at the old time step T_P^n, the liquid phase fraction at the last iteration f_P^k and the liquid phase fraction at the last time step f_P^n.

Finally, the liquid phase fraction corresponding to the new iterative level had to be calculated. Following Voller and Swaminathan [43], the liquid phase fraction f_P^{k+1} was calculated from the previous iteration value f_P^k, depending on if the node P was changing phase or not:

$$f_P^{k+1}$$
$$= f_P^k + \begin{cases} \dfrac{a_P \left(T_P^{k+1} - F^{-1}(f_P^k) \right)}{\rho_P L_P V_P} & f_P^k \leq 0, f_P^k \geq 1 \\[2ex] \dfrac{\partial F(T)}{\partial T} \left(T_P^{k+1} - F^{-1}(f_P^k) \right) & 0 < f_P^k < 1 \end{cases} \tag{63}$$

Now, there were two equations (62) and (63) for the temperature T_P^{k+1} and the liquid fraction f_P^{k+1} of interior nodes P.

At the boundary nodes, a constant heat flux source term was included,

$$S_b^{k+1} = -A_b {q''_{HTF}}^n, \qquad (64)$$

where, the heat flux value of the HTF from the last time step was multiplied with the boundary area. We did not linearize this source term, as the heat flux in the HTF depended on multiple temperatures and heat transfer coefficients.

3.3.3. Effective fin modelling

Although the structured cylindrical model allowed for efficient computation of the discretized radial plate fin, the branched axial fin cannot be discretized in detail with this method, because it is an unstructured geometry. Therefore, we developed an effective fin model that assumes an effective mixture material of the fins and the PCM. This model can be used to approximate any nearly cylindrical geometry on a structured cylindrical mesh. This also allows a coarser mesh and thereby significantly decreases the computational effort. In the following, our effective fin model is defined, which is adjusted to both fin designs in the results section 5.2. The geometry and discretization of a test case using the effective fin model are shown in Figure 7.

a) Arbitrary unstructured fin geometry

b) Effective cylindrical geometry

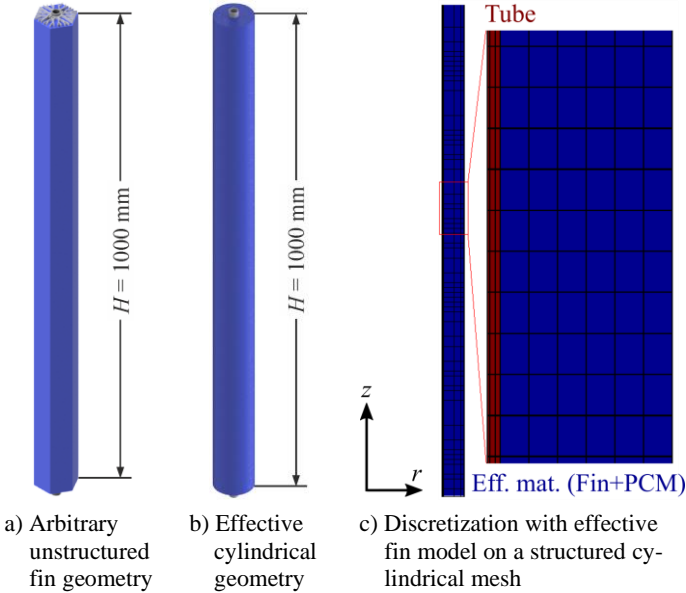c) Discretization with effective fin model on a structured cylindrical mesh

Figure 7: Geometry and discretization of a finned tube LTES system using the effective fin model on a structured cylindrical mesh.

For the geometry, an effective outer radius of the storage domain was calculated. The domain of the detailed geometry had a hexagonal shape due to a tube arrangement in triangles. But the effective model used a cylindrical 2D mesh. Therefore, an effective radius was defined:

$$R_{\text{storage,eff}} = \sqrt{\frac{A_{\text{hexagon}}}{\pi}} = \sqrt{\frac{\frac{\sqrt{3}}{2} D_t^2}{\pi}}. \qquad (65)$$

The circle with radius $R_{\text{storage,eff}}$ has the same area as the regular hexagon with height D_t, which is the tube distance D_t shown in Figure 1. Hence, the effective cylindrical geometry has the same volume as the original hexagonal geometry. The resulting radii for both fin designs are given in the results section in Table 8.

Our effective fin model is based on the calculation of mixture properties for an approximate analytical model described by Bauer [23]. First, the fin fraction is defined from the volumes of fin and PCM:

$$v_{\text{fin}} = \frac{V_{\text{fin}}}{V_{\text{fin}} + V_{\text{PCM}}} \qquad (66)$$

The fin fraction of the radial plate fin was $v_{\text{fin,plate}} = 0.083$. However, to increase the accuracy of the effective fin model for the radial plate fin, we defined two sub-regions, see Figure 5 b): the first was an inner mixture region containing the fins with outer radius $\tilde{R}_{\text{storage,eff}} = 0.046$. The second was the remaining outer part containing only PCM. The inner mixture region has a modified fin fraction $\tilde{v}_{\text{fin,plate}} = 0.109$. The fin fraction of the branched axial fin was $v_{\text{fin,branched}} = 0.179$ and it was calculated over the whole region of PCM and fin.

The effective density, specific heat capacity and latent heat were then calculated with respect to the fin fraction:

$$\begin{aligned} \rho_{\text{eff}} &= v_{\text{fin}}\rho_{\text{fin}} + (1 - v_{\text{fin}})\rho_{\text{PCM}}, \\ L_{\text{eff}} &= \frac{\rho_{\text{PCM}}}{\rho_{\text{eff}}}(1 - v_{\text{fin}})L_{\text{PCM}}, \\ c_{\text{eff}} &= \frac{\rho_{\text{fin}}}{\rho_{\text{eff}}}v_{\text{fin}}c_{\text{fin}} + \frac{\rho_{\text{PCM}}}{\rho_{\text{eff}}}(1 - v_{\text{fin}})c_{\text{PCM}}. \end{aligned} \qquad (67)$$

The effective thermal conductivity may be expressed either in a parallel or serial arrangement, which was described, among other methods, by Meshgin and Xi [24]:

$$\begin{aligned} k_{\text{eff,par}} &= v_{\text{fin}}k_{\text{fin}} + (1 - v_{\text{fin}})k_{\text{PCM}}, \\ \frac{1}{k_{\text{eff,ser}}} &= \frac{v_{\text{fin}}}{k_{\text{fin}}} + \frac{(1 - v_{\text{fin}})}{k_{\text{PCM}}}. \end{aligned} \qquad (68)$$

The parallel arrangement represents the mixture with the highest thermal conductivity and the serial arrangement that with the lowest thermal conductivity. The resulting effective material properties for the two examined fin designs are shown in Table 4.

Table 4: Thermo-physical material properties of the effective mixtures of PCM and fin materials for the two investigated fin designs.

Effective property	Unit	Radial plate: 89.1 % KNO₃ NaNO₃+ 10.9 % Al 6060	Branched axial: 82.1 % NaNO₃+ 17.9 % Al 6060
ρ_{eff}	$\frac{\text{kg}}{\text{m}^3}$	2040	2050
L_{eff}	$\frac{\text{kJ}}{\text{kg}}$	103.7	135.9
c_{eff}	$\frac{\text{J}}{\text{kg K}}$	1308 (sol) 1365 (liq)	1494 (sol) 1505 (liq)
$k_{\text{eff,par}}$	$\frac{\text{W}}{\text{m K}}$	23.36 (sol) 23.36 (liq)	38.24 (sol) 38.12 (liq)
$k_{\text{eff,ser}}$		0.5111 (sol) 0.5129 (liq)	0.8093 (sol) 0.6261 (liq)

The thermal conductivity of the effective fin k_{eff} must be in between the parallel arrangement $k_{\text{eff,par}}$ and the series arrangement $k_{\text{eff,ser}}$. Similarly, as described by Tay et al. [25], a weighted average can be defined introducing the factor of parallelism $P = 0 \dots 1$:

$$k_{\text{eff}} = Pk_{\text{eff,par}} + (1 - P)k_{\text{eff,ser}}. \qquad (69)$$

A suitable value of P led to a good approximation of a certain fin and PCM arrangement, at least when only one direction of heat conduction was regarded. However, fins can have different thermal conduction properties in different directions and the existing effective models did not yet resolve this. Therefore, we defined separate effective thermal conductivities in the radial and axial direction and determined two factors of parallelism P_r and P_z. The values of these parameters are presented in the results section 5.2 for both fin geometries. The effective thermal conductivity was then defined in the radial and the axial direction as well:

$$k_{r,\text{eff}} = P_r k_{\text{eff,par}} + (1 - P_r)k_{\text{eff,ser}},$$
$$k_{z,\text{eff}} = P_z k_{\text{eff,par}} + (1 - P_z)k_{\text{eff,ser}}. \tag{70}$$

Another important aspect was that an effective mixture of PCM and fin do not have a distinct melting point, because of the significant sensible heat content introduced by the fin material. Therefore, we defined an effective melting range δT_{eff} that had to be adjusted as well. The liquidus temperature $T_{\text{liq,eff}}$ and the solidus temperature $T_{\text{sol,eff}}$ of the effective material were defined as follows:

$$T_{\text{liq,eff}} = \begin{cases} T_{\text{liq}} + \delta T_{\text{eff}}, & \dot{Q} \geq 0 \\ T_{\text{liq}}, & \dot{Q} < 0 \end{cases},$$
$$T_{\text{sol,eff}} = \begin{cases} T_{\text{sol}}, & \dot{Q} \geq 0 \\ T_{\text{sol}} - \delta T_{\text{eff}}, & \dot{Q} < 0 \end{cases}. \tag{71}$$

This automatically gives a positive melting range during charging ($\dot{Q} \geq 0$) and a negative melting range during discharging ($\dot{Q} < 0$). Suitable values of the effective melting range δT_{eff} are given in the results section.

3.3.4. Solution procedure

Solving equation (62) for each grid node lead to a linear system of equations in the form

$$\boldsymbol{A} \cdot \boldsymbol{T}^{k+1} = \boldsymbol{B}, \tag{72}$$

which was solved in MATLAB with the function mldivide (invoked with the backslash operator). This function detects that the matrix $\boldsymbol{A}$ is symmetric and diagonal and applies a direct solver (CHOLMOD: Sparse Cholesky factorization and modification package), which lead to a fast and accurate solution.

The solution procedure for one iteration was as follows: 1) material values are updated, 2) boundary and liquid fraction source terms are updated, 3) coefficients of the linear system are calculated, 4) temperature field is obtained by solving the linear system (72), 5) liquid fraction is corrected by equation (63) and 6) derived quantities such as dimensionless variables are calculated.

This procedure was repeated until convergence was reached with the following criteria, which state that the L^2 norms of the absolute change of temperatures and liquid phase fractions from the last to the current iteration must fall below values of 10^{-6}:

$$\|T^{k+1} - T^k\|_2 < 10^{-6} \text{ K}, \qquad \|f^{k+1} - f^k\|_2 < 10^{-6} \tag{73}$$

Usually, only 2 to 3 iterations were needed for convergence of the solution due to the previously described linearized source-based scheme with an efficient direct solver for the system of linear equations.

4. Model coupling with iterative solution scheme

The previously described models for the HTF and the PCM+HEX were coupled with an iterative solution method. Both models already needed internal iterations due to their implicit nature. To couple the two models, an outer iterative scheme was developed, as depicted in Figure 8.
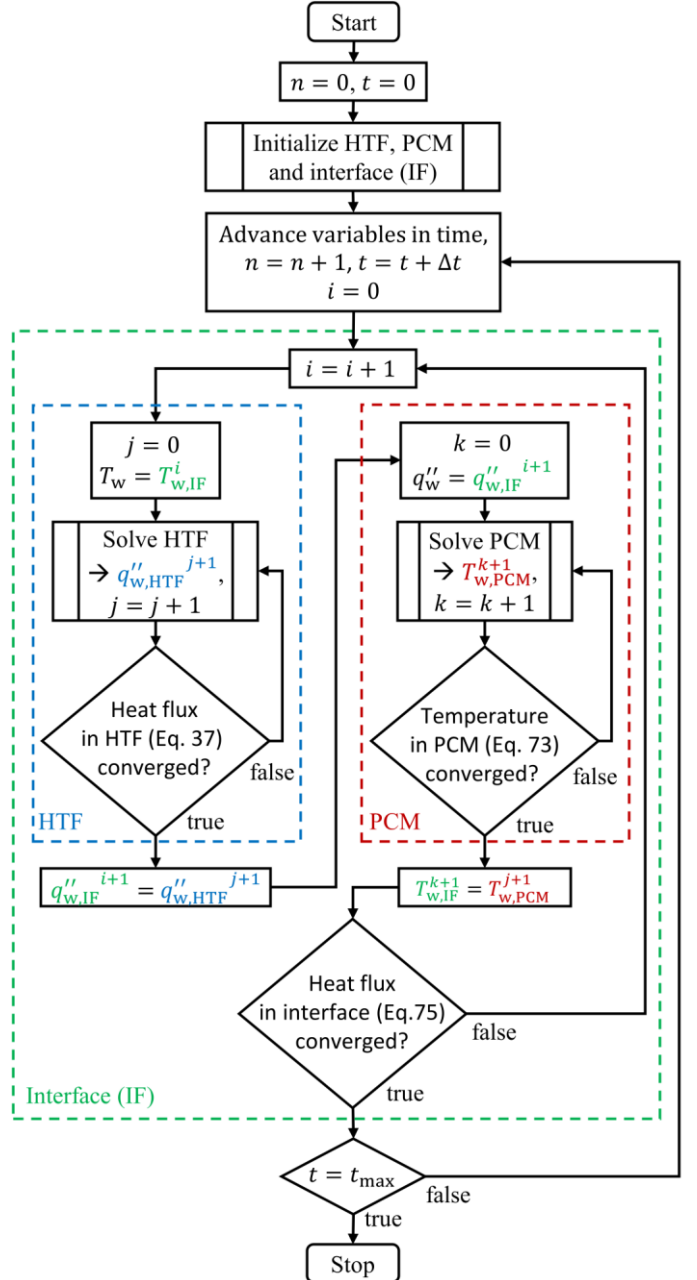

Figure 8: Flowchart for the iterative scheme solving the coupled simulation of the HTF and the PCM+HEX models using an interface (IF).

The first step was to initialize the models. Both models were programmed as classes. During initialization, object instances were created from the classes and the meshes were generated.

To connect the models, an interface object was used. The interface was used to store the boundary solution from both models and to determine convergence of the coupled solution. This approach had the advantage that the models could be used stand-alone or coupled. Also, the interface was used to couple different solution methods. The HTF model was always the same, as described in section 2 of this paper. But for the PCM+HEX, either the structured cylindrical model written in MATLAB was used or the unstructured model implemented in ANSYS Fluent was used. The interface class also contained programs for remote control of ANSYS Fluent with the "as a server" (AAS) functionality. This way, ANSYS Fluent could be started and configured out of MATLAB and a coupled solution could be obtained with both programs performing iterations and waiting for the solution of the coupled counterpart. However, the solution data at the boundaries could not be transferred over the remote-control libraries and had to be written to and read from ANSYS Fluent profile files.

After initialization, the solution variables are advanced in time, e.g. the temperature in the PCM+HEX model,

$$T^n = T^{j+1}, \tag{74}$$

where the converged result from the last time step T^{j+1} is stored as the old value of the current time step. Also, the number of the time step n and the time t are updated. The interface iterations are denoted with k, the HTF iterations with i and the storage iterations with j. The interface iterations begin with obtaining a solution of the HTF model. Therefore, the wall temperature is obtained from the interface. The block "solve HTF" includes the obtaining of the solution as described in section 2. The convergence is determined from the scaled change in heat flux as calculated in Equation (37). Iterations continue until the solution is converged. The heat flux is then written to the interface and the solution of the PCM+HEX begins with obtaining the heat flux from the interface. The block "solve PCM" includes the solution procedure as described in section 3. The. iterations continue until convergence is determined from equation (73). The resulting wall temperature is then written to the interface, a new wall heat flux is calculated and the convergence criterion for the interface, which is the relative change of wall heat flux from the last to the current interface iteration, is checked:

$$\left\| \frac{q_w''^{i+1} - q_w''^{i}}{q_w''^{i+1}} \right\|_2 < 10^{-2}. \tag{75}$$

The outer interface iterations, including inner iterations in the HTF and the PCM+HEX models, continue until the solution is converged. About 4 to 6 interface iterations are needed on average per time step, depending on the models used. After convergence, the criterion for exiting the temporal loop, $t = t_{max}$, is checked. The time steps continue until the maximum time is reached and the simulation is stopped.

5. Results and discussion

The results produced for this article were mainly intended to verify and adjust the presented models. Therefore, several test cases were defined as a basis for verification and bench-marking purposes. The following first part is about the verification of the HTF model by comparing results of a charging and a discharging test case with the commercial software package Apros®. The second part regards the calibration and verification of the effective fin model used in the self-tailored MATLAB code for a fast solving of the PCM+HEX domain. Simple test cases were defined, and the solutions were adjusted and compared to results obtained with the commercial software package ANSYS Fluent. The third part is about the verification of the coupled large-scale model. Two test cases with charging and discharging of two different storage systems were defined and solutions using the effective fin model were compared to solutions using the discretized fin models.

5.1. Verification of the heat transfer fluid (HTF) model

To verify the heat transfer fluid model, two reference test cases are used: one for charging and one for discharging. The tube, in which the HTF flows, has an inner diameter $R_{HTF} = 0.00775$ m and a height $H = 6$ m. It is discretized in one dimension with 61 nodes that are equally distributed over the height. The mass flow rate $\dot{m}$, pressure p and temperature T are given at the inlet, which is at the top of the tube during charging and at the bottom of the tube during discharging. The inlet pressure defines the saturation temperature T_{sat}. The thermal boundary condition for these reference test cases is a constant heat flux q_w'', applied to the outer tube surface. The parameters defining the test cases are given in Table 5.

Table 5: Definition of verification test cases for the HTF model during charging and discharging.

	Charging	Discharging
$\dot{m}_{Inlet}$ / kg/s	$-\dfrac{0.5}{152}$	$\dfrac{0.5}{152}$
p_{Inlet} / bar	107	81
T_{sat} / °C	316	296
T_{Inlet} / °C	330	287
q_w'' / W/m²	-16434	17535

We simulated the test cases with our model as well as with the commercial software Apros® and compared the pressure p, temperature T, void fraction α and heat transfer coefficient H. The charging case with condensation of superheated steam flowing downward from the top is shown in Figure 9. We observe that the pressure is well captured by the model compared to Apros® results. However, the pressure losses due to friction and acceleration are negligible and only the hydrostatic (gravitational) increase of pressure from the inlet at the top to the outlet at the bottom has a noticeable contribution. Still, this contribution is small, and the overall pressure change of $\Delta p = 0.06$ bar can be neglected in this test case. This may be different for larger flow velocities, longer tubes or larger regions of liquid phase. The wall temperatures T_w also compared well, while the fluid temperature T_f shows larger deviations in the upper half of the tube. This is because the Apros® model resolves the thin liquid film at saturation temperature and the superheated gas phase and then calculates a mixture temperature. But our simpler heterogeneous approach models both phases at a common equilibrium temperature, which can only be the saturation temperature during condensation. However,

the significant part of the condensation heat flux is calculated using only the wall temperature and the saturation temperature, which is why we don't need to resolve the fluid temperature during phase change. For the void fraction α, we obtained very similar values from our model compared to Apros® results. The heat transfer coefficient H calculated by our model shows a slight deviation in the superheated condensation region and the beginning of the saturated condensation at a height between $z \approx 5.3$ m and $z \approx 6$ m, but it does compare well to Apros® results in the remaining regions. The heat transfer coefficient in the condensation region during charging has a mean value of $H_C = 8\,641 \frac{\text{W}}{\text{m}^2\text{K}}$.
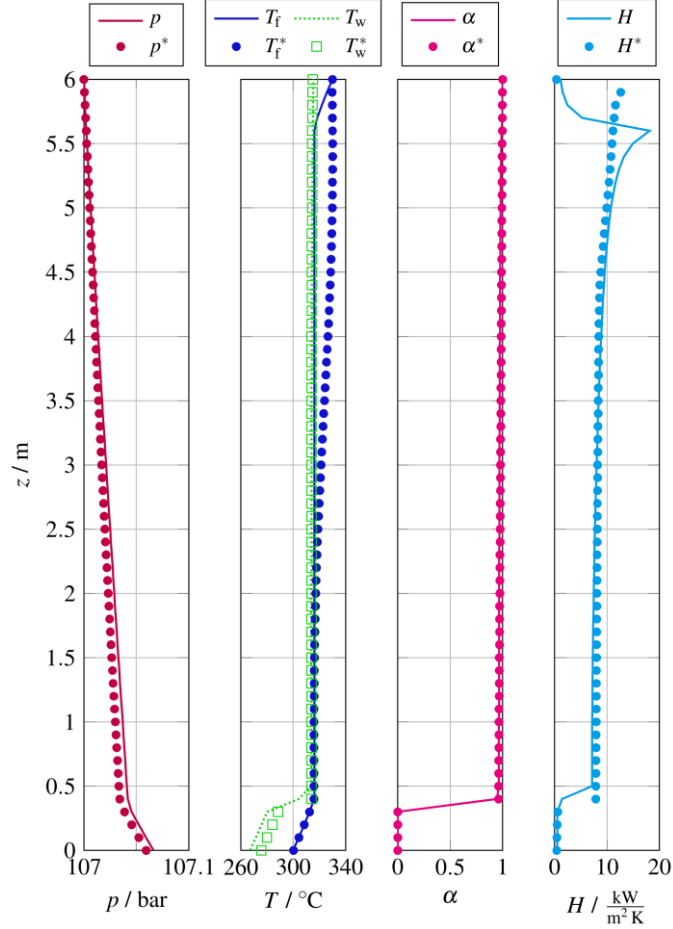
Figure 9: Verification test case of the HTF model during charging. The variables marked with an asterisk (*) are reference results obtained by Keller [20] using the commercial software Apros® [47].

The discharging case with boiling of subcooled water flowing upward from the bottom is shown in Figure 10. The pressure is again represented well by our model compared to Apros® results. A significant contribution to the pressure loss is again only due to the hydrostatic (gravitational) part between the inlet at the bottom and the outlet at the top. The pressure change $\Delta p = 0.24$ bar is considerably larger in this boiling test case compared to the condensation test case, which is due to a larger content of liquid phase in the tube, which leads to a larger density and therefore larger hydrostatic pressure change. Still, in this test case the pressure change is rather insignificant, which may change for different dimensions or boundary conditions. The temperatures of the fluid and the wall both agree very well compared with Apros® results. Also, the void fraction shows only minor deviations. Finally, the heat transfer coefficient calculated with our model agrees well with Apros® results, showing only minor deviations during subcooled boiling at $z \approx 0.2$ m. The heat transfer coefficient in the boiling region during discharging has a mean value of $H_B = 15\,005 \frac{\text{W}}{\text{m}^2\text{K}}$, which is significantly higher than during charging.
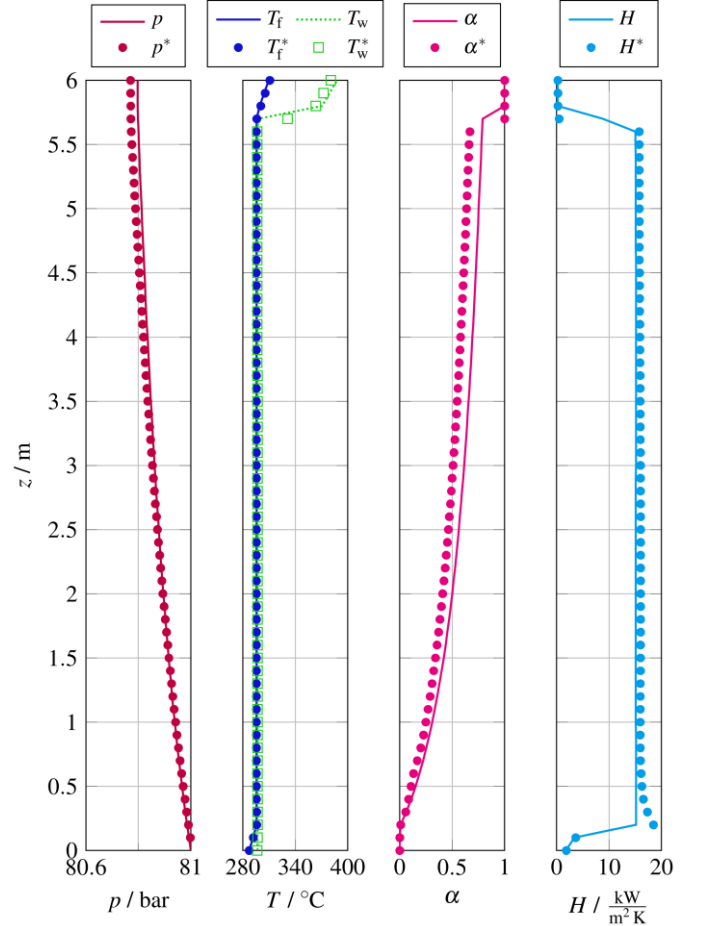

Figure 10: Verification test case of the HTF model during discharging. The variables marked with an asterisk (*) are reference results obtained by Keller [20] using the commercial software Apros® [47].

The main results are: firstly, the pressure change may be neglected in these and similar test cases. Secondly, the results from our simple heterogeneous model compare well to reference results obtained with Apros® for this test case.

5.2. Calibration and verification of the effective fin (EF) model

To define the effective fin model, the parameters for the factor of parallelism for thermal conductivity in radial and axial direction P_{radial} and P_{axial}, and the effective melting range δT_{eff} had to be determined. Therefore, different verification test cases were defined for both fin designs, as given in Table 6.

For each fin design, test cases for heat transfer in the radial and axial direction were set up. In these verification test cases, only heat transfer in the fin and PCM regions was investigated. The tube material was not included here, because it remained

fully discretized in the effective fin model and was therefore not contributing to the effective fin model properties.

Reference solutions were obtained with the discretized fin model for unstructured geometries, which was described in section 3.2. The verification test cases of the discretized fin model of the radial plate fin are illustrated in Figure 11 and that of the branched axial fin in Figure 12.

Table 6: Test cases for the parameter adjustment and verification of the effective fin model for the two fin designs and different driving temperature differences $\Delta T = T_{\mathrm{w}} - T_{\mathrm{m}}$. The discretized fin models serve as reference. The effective fin models are calibrated on the temperature difference marked with *, while the other temperature difference serves as extended verification test.

Fin design	Direction of heat transfer	$\Delta T/\mathrm{K}$	Discretized fin test cases	Effective fin test cases
Radial plate	Radial	50^*	R-DF-50	R-EF-50
	Axial	50^*	A-DF-50	A-EF-50
	Radial	25	R-DF-25	R-EF-25
	Axial	25	A-DF-25	A-EF-25
Branched axial	Radial	10^*	R-DF-10	R-EF-10
	Axial	10^*	A-DF-10	A-EF-10
	Radial	20	R-DF-20	R-EF-20
	Axial	20	A-DF-20	A-EF-20

a) Radial heat transfer with discretized fin model (R-DF)

b) Axial heat transfer with discretized fin model (A-DF)
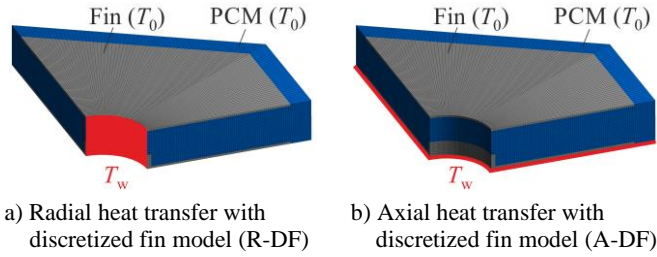
Figure 11: Discretized fin (DF) model of the radial plate fin for the verification test cases.

a) Radial heat transfer with discretized fin model (R-DF)

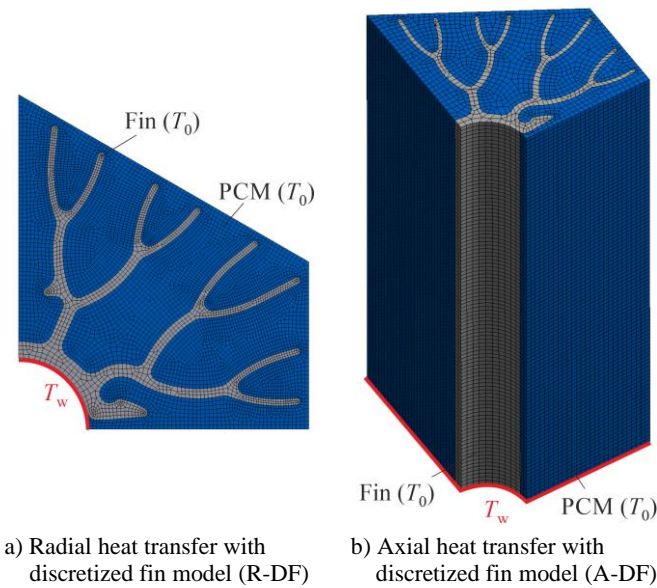b) Axial heat transfer with discretized fin model (A-DF)

Figure 12: Discretized fin (DF) model of the branched axial fin for the verification test cases.

The effective fin models, which were described in 3.3.3, have the same simplified cylindrical geometry for both fin designs shown in Figure 13.

a) Radial heat transfer with effective fin model (R-EF)

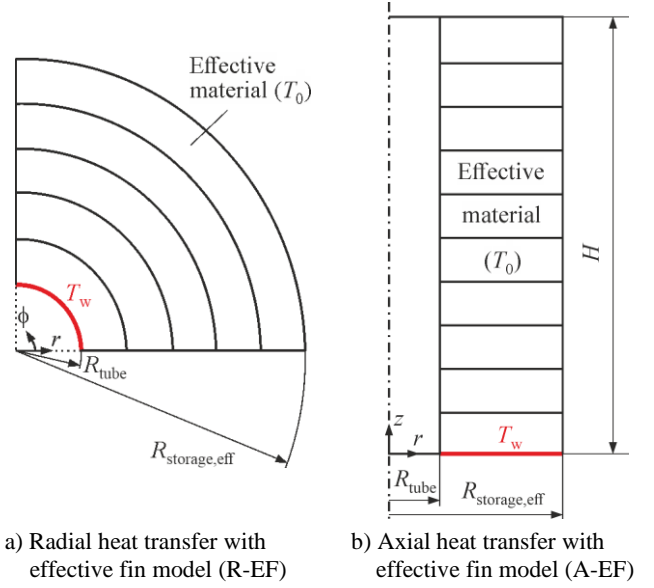b) Axial heat transfer with effective fin model (A-EF)

Figure 13: Effective fin (EF) models for the verification test cases.

The effective fin models were first calibrated to the discretized fin model using test cases with a certain driving temperature difference ΔT. A second set of test cases with another driving temperature difference served as extended verification test. The parameters of the effective fin model were optimized by trial and error. The goal was to obtain results from the effective fin model that qualitatively matched the results of the discretized fin model. The obtained parameters are presented in Table 7.

Table 7: Parameters adjusted to the verification test cases.

Parameter	Radial plate	Branched axial
Radial factor of parallelism P_r	0.8	0.7
Axial factor of parallelism P_z	0.006	1
Effective melting range δT_{eff}	12.5 K	5 K

From these results, we can learn that both fin types had a similar radial factor of parallelism, which indicated similar radial heat transfer enhancement capability. However, this property seemed to be slightly stronger for the radial plate fin compared to the branched axial fin. In the axial direction, a different picture was drawn. While the radial plate fin seemed to not enhance heat transfer in axial direction, the branched axial fin had a near optimal heat transfer enhancement in the axial direction. This is an interesting result that can be directly applied in storage design. The radial plate fin increases heat transfer only in the radial direction and retains the thermal insulation properties of the PCM in axial direction. This can be advantageous, if the storage should be kept in a partially charged state for a longer time. However, for maximum power and short charging cycles, the branched axial fin can be advantageous, since it transfers heat also in the axial direction. Also, branched axial fins with larger gaps between fins allow for natural convection that increases the heat transfer especially during charging, as shown by Vogel and Johnson [21].

The verification of the effective fin model for the radial plate fin test case is shown in Figure 14 and the verification of the branched axial fin is shown in Figure 15. The plots show the heat flow rate $\dot{Q}$, the liquid phase fraction f_l, and the mean relative temperature $\bar{T} - T_\mathrm{m}$.
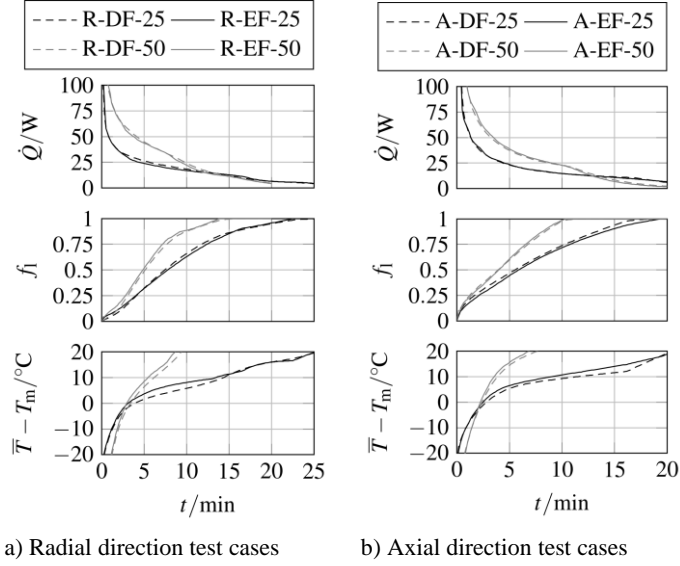

a) Radial direction test cases b) Axial direction test cases

Figure 14: Verification of the effective fin model for the heat exchanger design "Radial plate fin" calibrated for $\Delta T = 50$ K (grey lines). Another test case with $\Delta T = 25$ K (black lines) shows the scaling of the model outside of the calibrated range. Results of the effective fin (EF) model are shown in solid lines and results of the discretized fin (DF) model are shown in dashed lines.

a) Radial direction test cases b) Axial direction test cases
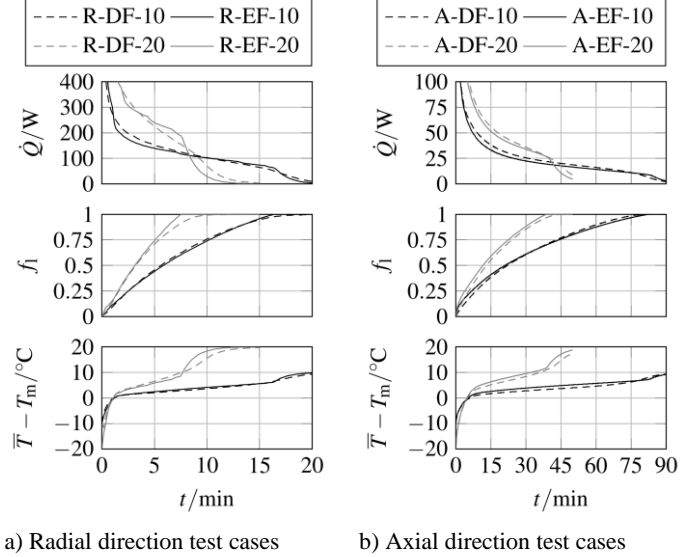
Figure 15: Verification of the effective fin model for the heat exchanger design "Branched axial fin" calibrated for $\Delta T = 10$ K (black lines). Another test case with $\Delta T = 20$ K (grey lines) shows the scaling of the model outside of the calibrated range. Results of the effective fin (EF) model are shown in solid lines and results of the discretized fin (DF) model are shown in dashed lines.

We observed a satisfactory agreement of the effective model with the discretized model for all the analyzed variables and for both driving temperature differences. The melting processes with both models are illustrated with contours of relative tem-

perature $T - T_\mathrm{m}$: Figure 16 shows the radial plate fin and Figure 17 shows the branched axial fin.

a) Radial case, discretized fin, $\Delta T = 50$ K (R-DF-50) b) Axial case, discretized fin, $\Delta T = 50$ K (A-DF-50)

c) Radial case, effective fin, $\Delta T = 50$ K (R-EF-50) d) Axial case, effective fin, $\Delta T = 50$ K (A-EF-50)
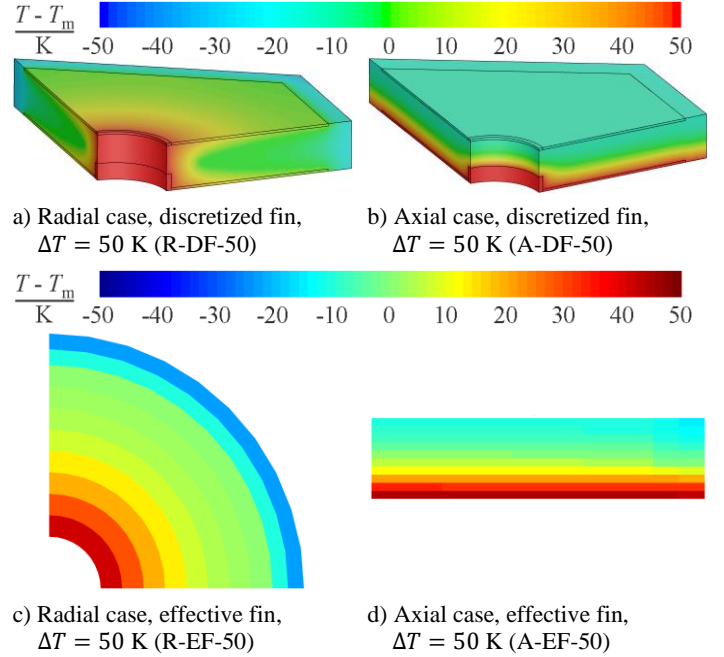
Figure 16: Contours of relative temperature $T - T_\mathrm{m}$ at $t = 200$ s in the verification test cases for radial and axial heat transfer of the discretized fin model and the effective fin model for the heat exchanger design "radial plate fin".
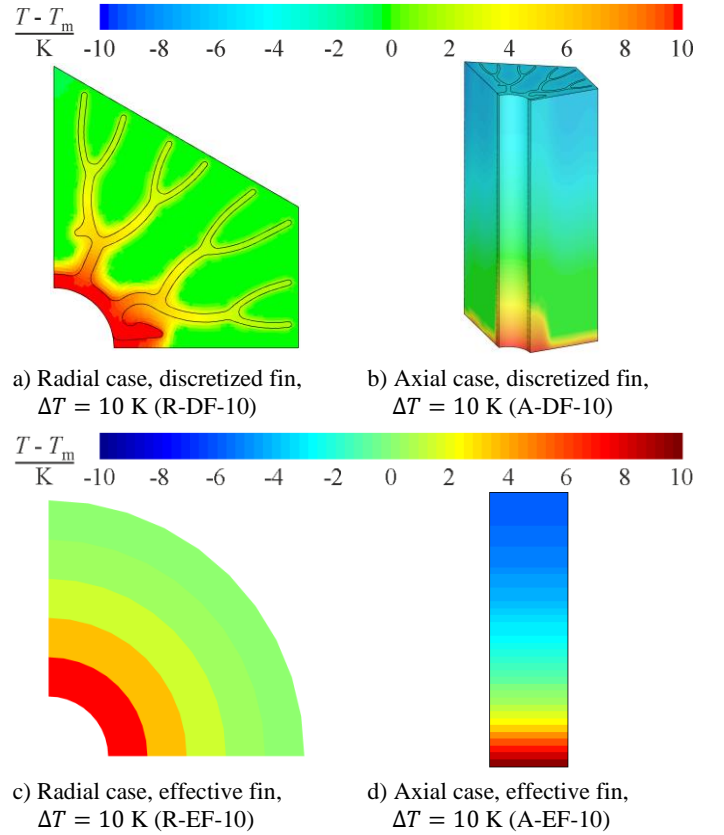

a) Radial case, discretized fin, $\Delta T = 10$ K (R-DF-10) b) Axial case, discretized fin, $\Delta T = 10$ K (A-DF-10)

c) Radial case, effective fin, $\Delta T = 10$ K (R-EF-10) d) Axial case, effective fin, $\Delta T = 10$ K (A-EF-10)

Figure 17: Contours of relative temperature $T - T_\mathrm{m}$ at $t = 200$ s in the verification test cases for radial and axial heat transfer of the discretized fin model and the effective fin model for the heat exchanger design "branched axial fin".

17

These plots reveal that the coarse approximation of the effective model represents the discretized model in a mean sense. While the temperature variation in the discretized fin model was captured with many computational control volumes, the same temperature variation is captured in the effective fin model with a larger effective melting range δT_{eff}. The different heat transfer properties of the fins in the radial and the axial directions were implemented with different thermal conductivities in these directions, which were calculated from a combination of the simple series and parallel arrangements of the materials. From these results, we concluded that the effective fin model was successfully calibrated and verified, showing good agreement with the discretized fin model. Therefore, the effective fin model was qualified to be used in the simulation of the full large-scale storage system.

5.3. Verification of the effective fin model at large scale

In the last two sections, we verified the model of the heat transfer fluid, and adjusted and verified the effective fin model for the storage part. However, the effective fin model must also prove to be accurate in the large-scale model, which couples the two sub-models and leads to temporally and spatially varying boundary conditions for the storage part. Therefore, we developed another two benchmark test cases of vertical shell-and-tube systems to test and verify the effective fin model. The properties of the two test cases are compiled in Table 8.

Table 8: Definition of two benchmark test cases for the coupled large-scale model.

	plate-1Ph	axial-2Ph
Fin design	Radial plate	Branched axial
HTF	Thermal oil Syltherm 800	Water/Steam IAPWS-IF97
PCM	KNO$_3$-NaNO$_3$ (T_m = 222 °C)	NaNO$_3$ (T_m = 306 °C)
Tube distance D_t / mm	100	70
Height H / mm	1000	1000
Fin volume fraction v_{fin}	8.28 %	17.95 %
R_{HTF} / mm	7.45	6.3
R_{tube} / mm	10.65	8.6
$R_{\text{storage,eff}}$ / mm	52.5	36.8
T_{ini}	$T_m - 50$ K	$T_m - 15$ K
$\dot{m}_{\text{Inlet}}$ / kg/s	0.02	0.00025
$p_{\text{Inlet,charging}}$ / bar	-	106.984
$p_{\text{Inlet,discharging}}$ / bar	-	81.1415
$T_{\text{sat,charging}}$	-	$T_m + 10$ K
$T_{\text{sat,discharging}}$	-	$T_m - 10$ K
$T_{\text{Inlet,charging}}$	$T_m + 50$ K	$T_m + 15$ K
$T_{\text{Inlet,discharging}}$	$T_m - 50$ K	$T_m - 15$ K

In the first test case, radial plate fins, see Figure 1 a), and thermal oil as a single-phase heat transfer fluid were used. In the second test case, axial fins, see Figure 1 b), and water/steam as a two-phase heat transfer fluid were used. The charging and discharging processes with water/steam as two-phase heat transfer fluid are illustrated in Figure 18.

a) Charging (condensation in HTF and melting in PCM)

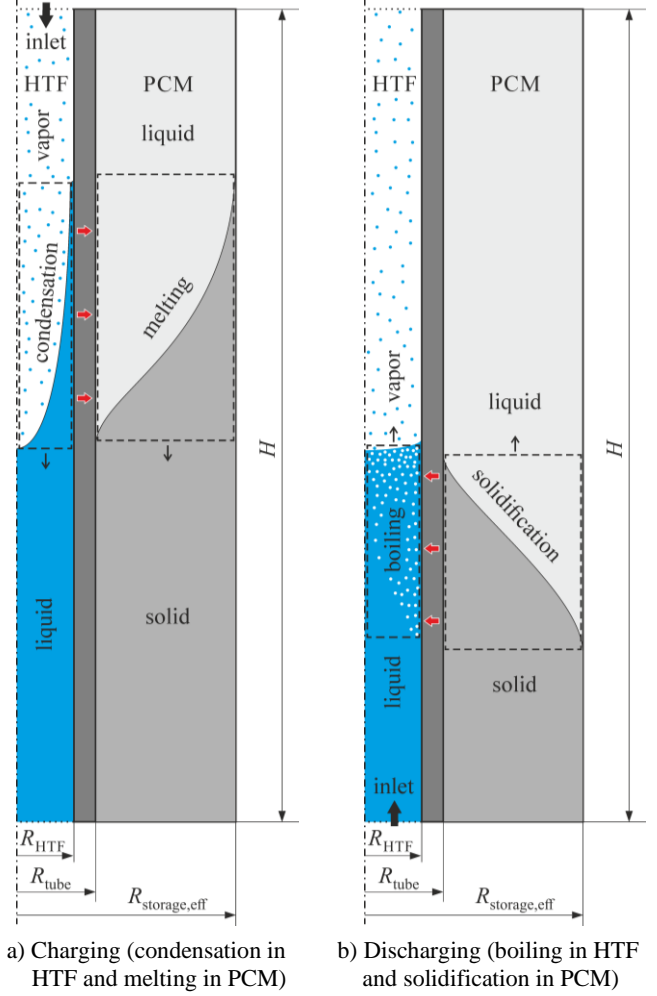b) Discharging (boiling in HTF and solidification in PCM)

Figure 18: Illustration of the charging and discharging processes in latent heat storage with two-phase flow in vertical tubes. The illustration is simplified according to the effective fin model. Therefore, fins are not shown and the domain is represented in cylindrical coordinates with a symmetry axis on the left.

5.3.1. Test case: plate-1Ph

The first test case "plate-1Ph" incorporated the radial plate fins, see Figure 1 a), and thermal oil as a single-phase heat transfer fluid. The parameters of the test case are given in Table 8. We ran simulations of a cycle including charging and discharging using both the effective fin (EF) model and the discretized fin (DF) model. The EF model used adjusted mixture properties of the HEX and the PCM as obtained in section 5.2 and was discretized on a coarse mesh as described in section 3.3. The DF model discretized the actual geometry of both the HEX and PCM materials, as described in section 3.2. The charging and discharging processes were set to a fixed duration of 4 h each, which led to a cycle duration of 8 h. The results are shown in Figure 19, where the heat transfer rate $\dot{Q}_w$, the liquid phase fraction f and the temperatures at the top and bottom of the HTF, $T_{\text{HTF,top}}$ and $T_{\text{HTF,bot}}$, respectively, are plotted over time for both models.
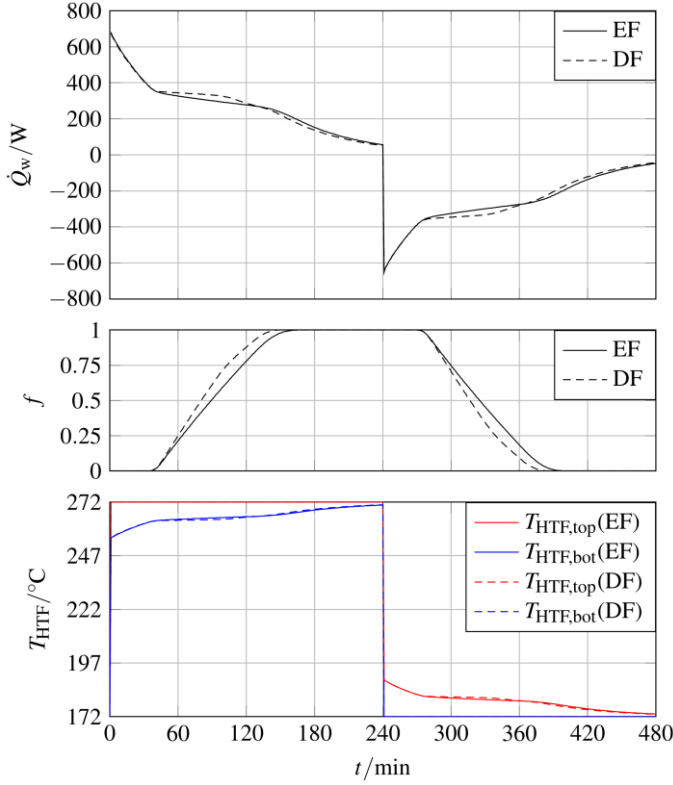
Figure 19: Comparison of the effective fin (EF) model to the discretized fin (DF) model of test case plate-1Ph. While charging, $T_{HTF,top}$ is the inlet temperature of the hot HTF at the top of the tube and $T_{HTF,bot}$ is the outlet temperature of the cooled HTF at the bottom of the tube. While discharging, $T_{HTF,bot}$ is the inlet temperature of the cold HTF at the bottom of the tube and $T_{HTF,top}$ is the outlet temperature of the heated HTF at the top of the tube.

The results indicate a qualitative agreement of the EF and DF models. Slight deviations can be observed during phase change, while the results are identical in sections without phase change. We quantitatively assessed the deviations using three different error metrics: the Mean Bias Error (MBE), the Mean Absolute Error (MAE) and the Root Mean Square Error (RMSE):

$$MBE = \frac{1}{N}\sum_{i=1}^{N}\left(y_{EF}\left(t_i\right) - y_{DF}\left(t_i\right)\right)$$

$$MAE = \frac{1}{N}\sum_{i=1}^{N}\left|y_{EF}\left(t_i\right) - y_{DF}\left(t_i\right)\right| \qquad (76)$$

$$RMSE = \sqrt{\frac{1}{N}\sum_{i=1}^{N}\left(y_{EF}\left(t_i\right) - y_{DF}\left(t_i\right)\right)^2}$$

The resulting metrics for the wall heat flow rate, the liquid phase fraction and the sum of HTF temperatures are given in Table 9.

Table 9: Deviations between the discretized fin (DF) and the effective fin (EF) models for the test case plate-1Ph.

| Error metric	$\dot{Q}_w$	f	$T_{HTF,top} + T_{HTF,bot}$
MBE	-0.004 W	-0.0006	-0.0008 K
MAE	14 W	0.03	0.2 K
RMSE	16 W	0.05	0.4 K

The MBE is low, because subsequent over- and underpredictions in the charging and discharging sections, or within a phase change process cancel out, which indicates conservation of the variables. The MAE takes the absolute values of deviations and thus adds up all the positive and negative deviations. Finally, the RMSE is larger as it weighs large deviations more than small deviations. In conclusion, deviations are sufficiently low to state that the results agree and the effective model is verified for this test case. To discuss the benefit in computational effort, both the spatial and temporal discretization parameters, as well as the CPU times, are given in Table 10.

Table 10: Discretization and CPU time for the discretized fin (DF) and the effective fin (EF) models in the test case plate-1Ph.

Value/Result	Discretized fin (DF)	Effective fin (EF)
# cells HTF	900	101
# cells HEX+PCM	18,000	1,313
time step Δt	60 s	60 s
time steps N	480	480
CPU time	150 s	30 s

Both models used the same MATLAB framework and discretization on structured cylindrical grids. The CPU time needed by using the effective fin (EF) model is only 20 % of that needed by the discretized fin (DF) model. And the effective fin model allows to arbitrarily coarsen the grid to reduce computational effort. This way, the effective fin model can easily scale to larger dimensions or even coarser discretization, where the discretized fin model would become unfeasible.

For visualization of the different models, a state during the charging cycle is illustrated in Figure 20. The temperatures T of the wall and the HTF, the heat transfer coefficient H and the wall heat flux q_w'' are plotted for the HTF region. Due to the single-phase heat transfer, there is a slight and continuous variation of the HTF properties along the z-axis. For the storage region, filled contours of the temperatures T and liquid phase fraction f are plotted, where results from the effective fin (EF) model and the discretized fin (DF) model are compared. As the temperature is around the melting point during phase change, there is not much information contained in the temperature plots. Rather, the state of charging is characterized by the liquid phase fraction f. The effective fin model seems to represent the phase state in a coarse mean sense, as already seen in section 5.2. While we cannot see the detailed phase state in the effective fin model, it is clear to see that melting is slightly faster at the top than at the bottom during charging, because the HTF enters at the top and cools flowing downward. During discharging, which is not shown, solidification is slightly faster at the bottom, because the flow direction is reversed. Hence, the effective model, while reduced in complexity, still gives a coarse state of temperatures and liquid phase fractions within the storage region.

19
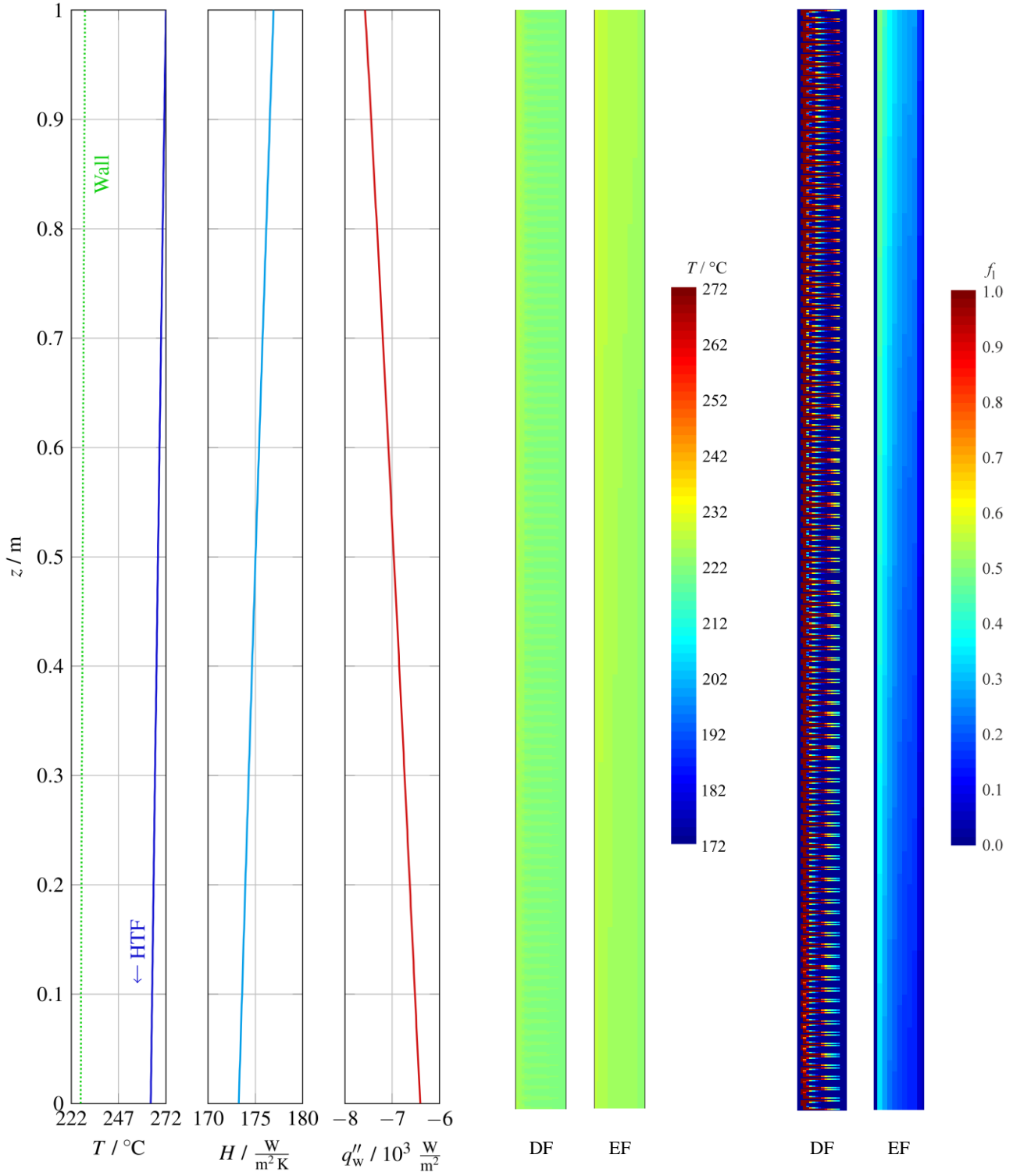
Figure 20: State during charging in cycle at time $t = 60$ min of test case plate-1Ph. In the HTF part, the temperatures T of the wall and the HTF, the heat transfer coefficient H and the wall heat flux q''_w are plotted over the vertical z-coordinate. In the storage part, the temperature T and liquid phase fraction f are plotted in the two-dimensional domain spanned by the vertical z-coordinate and the horizontal r-coordinate. The storage part is shown with both the effective fin (EF) model and the discretized fin (DF) model.

5.3.2. Test case: axial-2Ph

In the second test case "axial-2Ph", the branched axial fins, see Figure 1 b), and water as a two-phase heat transfer fluid were used. The parameters of the test case are given in Table 8.

For the coupled model, constant values should be used for the boiling and condensation heat transfer coefficients H_B and H_C of the HTF, see section 2.3.5. These values must be appropriately calculated beforehand with correlations suitable for the specific test case. For simplicity, and only for this verification

20

test case for the effective fin model, we chose values of the order of magnitude typically found in LTES systems:

$$H_B = H_C = 10{,}000. \tag{77}$$

We ran simulations of a cycle including charging and discharging using both the effective fin (EF) model and the discretized fin (DF) model. The charging and discharging processes were set to a fixed duration of 2 h each, which led to a cycle duration of 4 h. The results are shown in Figure 21, where the heat transfer rate $\dot{Q}_w$, the liquid phase fraction f and the temperatures at the top and bottom of the HTF, $T_{HTF,top}$ and $T_{HTF,bot}$, respectively, are plotted over time for both models.
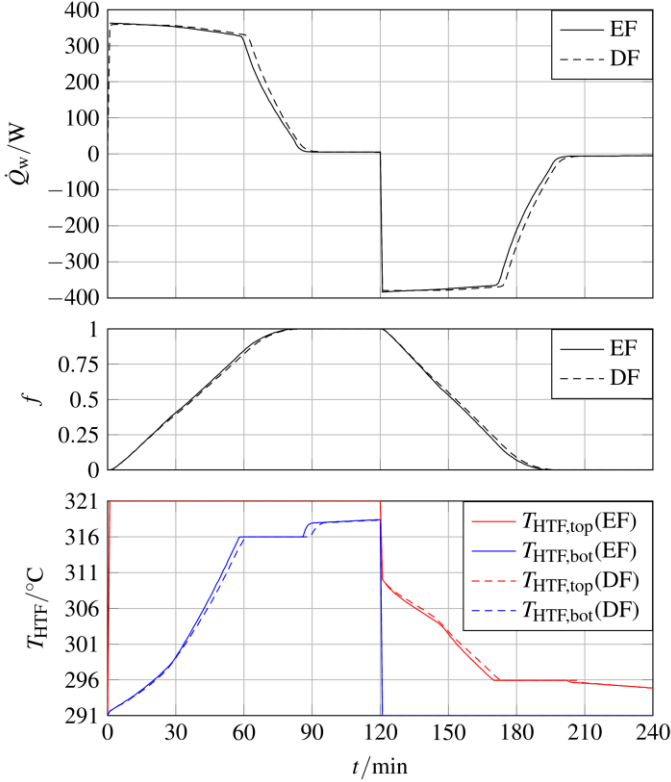
Figure 21: Comparison of the effective fin (EF) model to the discretized fin (DF) model of test case axial-2Ph. While charging, $T_{HTF,top}$ is the inlet temperature of the hot HTF at the top of the tube and $T_{HTF,bot}$ is the outlet temperature of the cooled HTF at the bottom of the tube. While discharging, $T_{HTF,bot}$ is the inlet temperature of the cold HTF at the bottom of the tube and $T_{HTF,top}$ is the outlet temperature of the heated HTF at the top of the tube.

The results indicate a qualitative agreement of the effective fin model with the discretized fin model for this test case. The error metrics were calculated from equation (76) as in the last section and the results are given in Table 11.

Table 11: Deviations between the discretized fin (DF) and the effective fin (EF) models for the test case axial-2Ph.

Error metric	$\dot{Q}_w$	f	$T_{HTF,top} + T_{HTF,bot}$
MBE	0.5 W	-0.001	0.05 K
MAE	8.2 W	0.008	0.2 K
RMSE	15 W	0.01	0.5 K

The error metrics indicate a larger bias (MBE) in this case compared to the previous case. However, all the metrics again

have sufficiently low values and indicate good agreement between the models. In conclusion, the EF model is verified for the test case axial-2Ph. The spatial and temporal discretization parameters, as well as the CPU times for this test case are given in Table 12.

Table 12: Discretization and CPU time for the discretized fin (DF) and the effective fin (EF) models in the test case axial-2Ph.

Value/Result	Discretized fin (DF)	Effective fin (EF)
# cells HTF	101	101
# cells PCM+HEX	134,300	909
time step Δt	5 s	5 s
time steps n	2,880	2,880
CPU time	32 h (4 cores)	320 s (1 core)

In this case, the effective fin (EF) model used the same MATLAB framework and discretization on structured cylindrical grids as in the previous test case. The discretized fin (DF) model used the MATLAB framework only for the HTF and used ANSYS Fluent in the storage part to discretize the HEX and the PCM of the branched axial fin geometry. The CPU time needed by using the EF model with one CPU core is 0.3 % of that needed by the DF model with all available 4 CPU cores. The high amount of CPU time needed by the DF model is mostly due to the demand of many computational cells and an unstructured solver. In this case, the effective fin model is the only efficient way to scale to larger dimensions, because the discretized fin model is already at its feasibility limit.

Similarly as in the last section, two states during charging and discharging are illustrated in Figure 22 and Figure 23, respectively. The temperatures T, the heat transfer coefficient H and the wall heat flux q''_w are plotted for the HTF region. With two-phase heat transfer, the heat transfer coefficient is highly discontinuous, with large values during boiling and condensation, and relatively low values in the adjacent regions of forced convection in the liquid or vapor. During charging, this results in a region of high heat transfer due to condensation that is initially at the top and gradually moves downward as melting progresses. During discharging, a region of high heat transfer due to boiling is initially at the bottom and gradually moves upward as solidification progresses. An interesting feature of such a storage system is that, due to the moving phase boundaries, the heat transfer rate remains at a relatively constant level during phase change, as seen in Figure 21.

As stated in section 2.3.5, we used constant and equal heat transfer coefficients for boiling and condensation. This was for the single purpose of simplicity and reproducibility of the verification test cases. Simulating a real storage system, the boiling and condensation heat transfer coefficients and the charging and discharging processes may be more dissimilar.

Having a closer look at the storage sides of Figure 22 and Figure 23, we observe that the EF model does not capture the detailed three-dimensional fields of temperature and liquid phase fraction around the fins as the DF model does. However, the EF model reproduces the vertical and radial variation of these variables and thus provides a clear picture of the general phase change process in the storage region. Conclusively, the effective fin model accurately predicts global quantities, such as the heat flow rate, with drastically reduced computational

effort, while it still provides a coarse state of internal temperatures and liquid phase fractions within the storage region. As a result, the presented EF model allows parameter and design studies of similar large-scale LTES systems, which have the possible outcome of increasing the efficiency and reducing the costs of such systems.
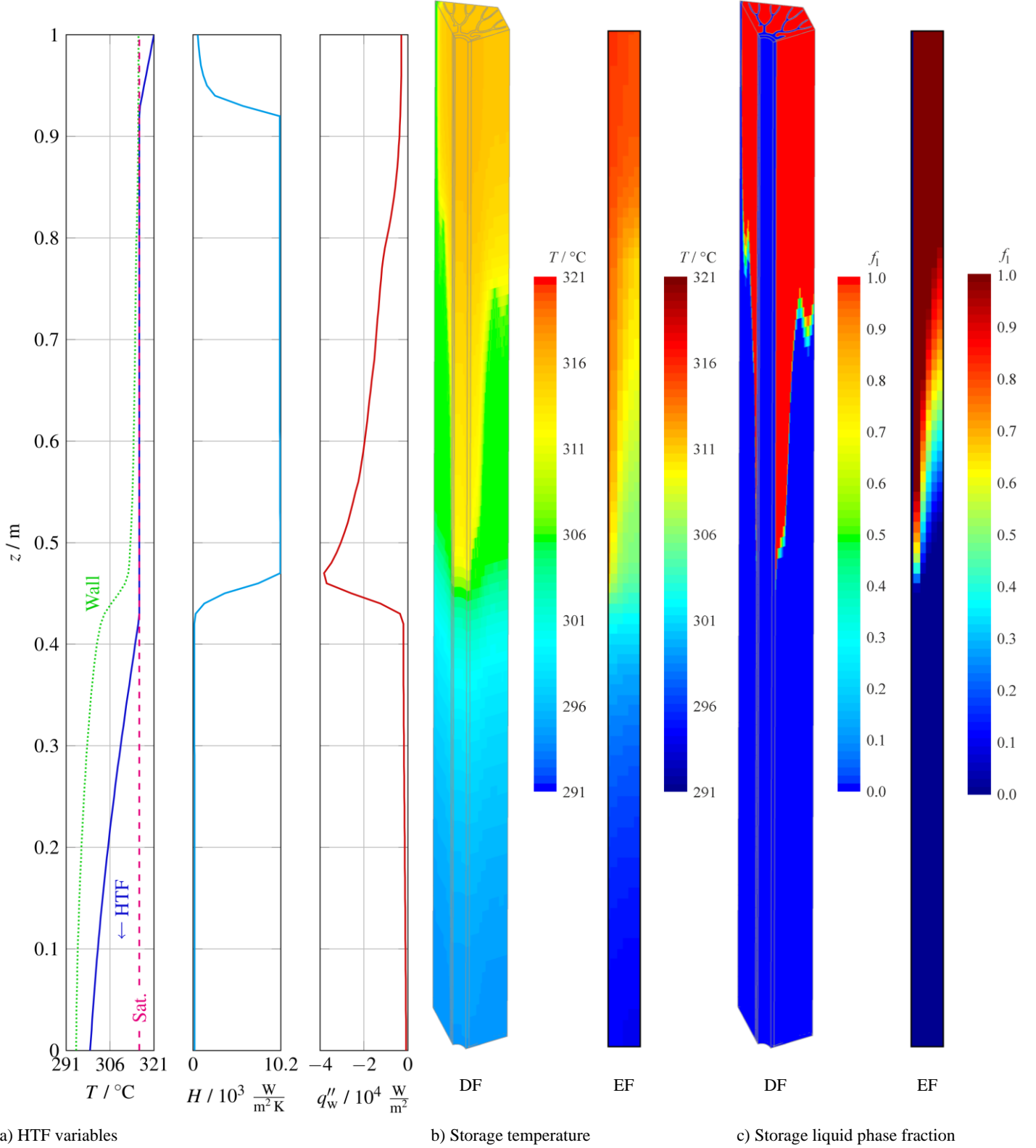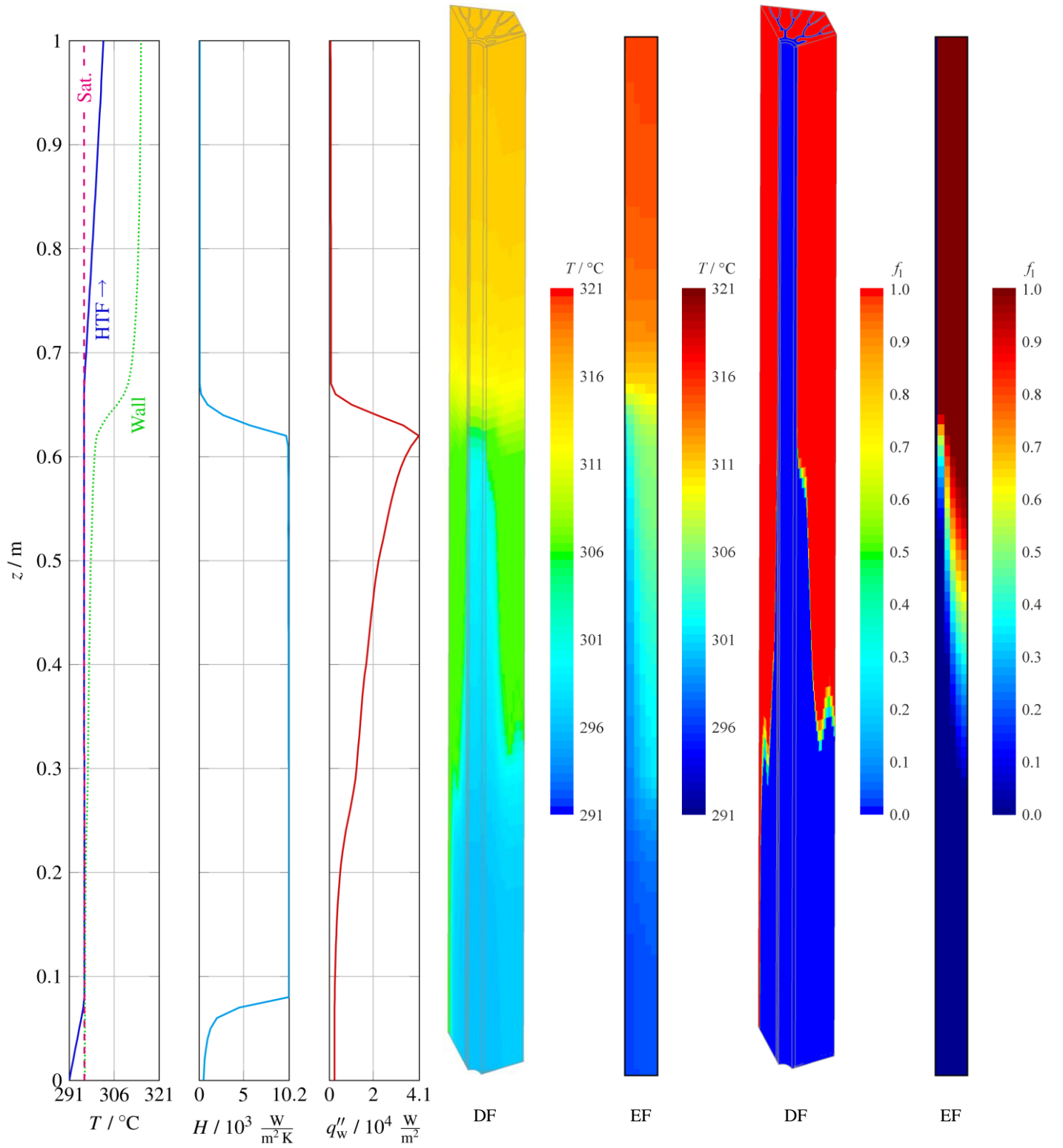

Figure 22: State during charging in cycle at time $t = 30$ min of test case axial-2Ph. In the HTF part, the temperatures T of the wall, the HTF and at saturation, the heat transfer coefficient H, and the wall heat flux q_w'' are plotted over the vertical z-coordinate. In the storage part, the temperature T and liquid phase fraction f are plotted in the three- or two-dimensional domains of the discretized fin (DF) model and the effective fin (EF) model.

a) HTF variables   b) Storage temperature   c) Storage liquid phase fraction

22

a) HTF variables   b) Storage temperature   c) Storage liquid phase fraction

Figure 23: State during charging in cycle at time $t = 150$ min of test case axial-2Ph. In the HTF part, the temperatures T of the wall, the HTF and at saturation, the heat transfer coefficient H, and the wall heat flux q_w'' are plotted over the vertical z-coordinate. In the storage part, the temperature T and liquid phase fraction f are plotted in the three- or two-dimensional domains of the discretized fin (DF) model and the effective fin (EF) model.

6. Conclusions and outlook

This research article presents an approach to build a large-scale model that includes the coupled transient heat transfer between the HTF and the storage region (PCM and HEX). A detailed discretized fin (DF) model of the storage region was replaced by an effective fin (EF) model to reduce the computational effort and allow for efficient large-scale simulations.

In the results of this article, three verification studies were performed. In the first part, the HTF model was compared to results with the commercial software Apros®. The first conclusion was that the small pressure change found in the presented test cases may be neglected. Another conclusion was that temperatures and heat transfer coefficients compared well to reference results obtained with Apros®. The HTF model was therefore accurate enough to be used for large-scale simulations. In the second verification study, the effective fin models were compared to discretized fin models for reference test cases of the storage part. The results indicated that the effective fin model represents the discretized fin model in a mean sense: while the discretized fin model captured the temperature variation with many computational control volumes, the effective fin model captured the same temperature variation with an effective melting range. The different heat transfer properties of the fins in radial and axial directions were implemented with different thermal conductivities in these directions, which were calculated from a combination of the series and parallel arrangements of the materials. The results indicated that the calibrated effective fin model was successfully verified for the reference test cases. The third verification study put the effective fin model to a practical test. Two realistic test cases were defined. The first included a radial plate fin and thermal oil as a single-phase heat transfer fluid. The second included a branched axial fin and water as a two-phase heat transfer fluid. A cycle including charging and discharging was defined for each test case. Both the effective fin model and the discretized fin model were used to simulate the test cases and the results indicated negligible deviations between the models. However, the computational effort with the EF model was significantly reduced: The CPU time of the first test case was 20 % and that of the second test case was 0.3 %, compared to the DF model. While reducing complexity, the EF model still provides a coarse state of internal temperatures and liquid phase fractions within the storage region.

In conclusion, the effective fin model described in this article leaded to accurate results. It allowed for fast large-scale modeling of vertical finned tube latent thermal energy storage systems. This enables parameter and design studies, which have the potential to increase efficiency and reduce costs.

Our outlook is as follows: The effective fin model can be calibrated to various fin types. Once a fin type is calibrated, parameter studies may be performed, altering the storage dimensions, material properties and boundary conditions. As our model is calculated directly from the material and heat transfer properties of a specific fin type, they remain valid in a certain parameter range. This way, LTES systems may be adjusted to different applications to optimize their performance, cost and sustainable material use. The finned tube height can be further increased to 12 m or more without excessive computational effort; in the present study we only chose smaller dimensions for illustration purpose. Additional physical effects, such as natural convection or close-contact melting, may be implemented to increase the general model accuracy.

References

[1]   IPCC. Climate Change 2014: Synthesis Report. Geneva, Switzerland: 2014.

[2]   International Energy Agency (IEA). Technology Roadmap: Energy storage. 2014.

[3]   Cabeza LF. Advances in Thermal Energy Storage Systems. Amsterdam: Woodhead Publishing; 2015. doi:10.1016/C2013-0-16453-7.

[4]   Laing D, Bauer T, Breidenbach N, Hachmann B, Johnson M. Development of high temperature phase-change-material storages. Appl Energy 2013;109:497–504. doi:10.1016/j.apenergy.2012.11.063.

[5]   Walter H, Beck A, Hameter M. Transient Analysis of an Improved Finned Tube Heat Exchanger for Thermal Energy Storage System. Proc. ASME 2015 9th Int. Conf. Energy Sustain., 2015, p. 1–14.

[6]   Olcese M, Couturier R, Fourmigue JF, Garcia P, Raccurt O, Robin JF, Senechal B, Rougé S, Thonon B. Design Methodology and Experimental Platform for the Validation of PCM Storage Modules for DSG Solar Plants. Energy Procedia 2014;49:945–55. doi:https://doi.org/10.1016/j.egypro.2014.03.102.

[7]   Feldhoff JF, Schmitz K, Eck M, Schnatbaum-Laumann L, Laing D, Ortiz-Vives F, Schulte-Fischedick J. Comparative system analysis of direct steam generation and synthetic oil parabolic trough power plants with integrated thermal storage. Sol Energy 2012;86:520–30. doi:10.1016/j.solener.2011.10.026.

[8]   Laing D, Bauer T, Lehmann D, Bahl C. Development of a Thermal Energy Storage System for Parabolic Trough Power Plants With Direct Steam Generation. Proc. ASME 2009 3rd Int. Conf. Energy Sustain., 2009.

[9]   Johnson M, Vogel J, Hempel M, Hachmann B, Dengel AJ. Design of High Temperature Thermal Energy Storage for High Power Levels. Sustain Cities Soc 2017;35:1–6. doi:10.1016/j.scs.2017.09.007.

[10]   Agyenim F, Hewitt N, Eames P, Smyth M. A review of materials, heat transfer and phase change problem formulation for latent heat thermal energy storage systems (LHTESS). Renew Sustain Energy Rev 2010;14:615–28.

doi:10.1016/j.rser.2009.10.015.

[11] Jegadheeswaran S, Pohekar SD. Performance enhancement in latent heat thermal storage system: A review. Renew Sustain Energy Rev 2009;13:2225–44. doi:10.1016/j.rser.2009.06.024.

[12] Agyenim F, Eames P, Smyth M. A comparison of heat transfer enhancement in a medium temperature thermal energy storage heat exchanger using fins. Sol Energy 2009;83:1509–20. doi:10.1016/j.solener.2009.04.007.

[13] Liu M, Saman W, Bruno F. Review on storage materials and thermal performance enhancement techniques for high temperature phase change thermal storage systems. Renew Sustain Energy Rev 2012;16:2118–32. doi:10.1016/j.rser.2012.01.020.

[14] Gasia J, Miró L, Cabeza LF. Materials and system requirements of high temperature thermal energy storage systems: A review. Part 2: Thermal conductivity enhancement techniques. Renew Sustain Energy Rev 2016;60:1584–601. doi:10.1016/j.rser.2016.03.019.

[15] Whalley PB. Two-phase flow and heat transfer. Oxford University Press; 1996.

[16] Ghiaasiaan S. Two-phase flow, boiling, and condensation: in conventional and miniature systems. 2008.

[17] Baehr HD, Stephan K. Wärme- und Stoffübertragung. Berlin, Heidelberg: Springer Berlin Heidelberg; 2013. doi:10.1007/978-3-642-10194-6.

[18] VDI Heat Atlas (VDI Wärmeatlas). Berlin, Heidelberg: Springer Verlag; 2013. doi:10.1007/978-3-642-19981-3.

[19] Sun K, Duffey R, Peng C. The prediction of two-phase mixture level and hydrodynamically-controlled dryout under low flow conditions. Int J Multiph Flow 1981;7:521–43.

[20] Keller M. Modellierung der Zweiphasenströmung in senkrechten Rohren für die Anwendung von PCM-Speichern in solarthermischen Kraftwerken mit Direktverdampfung. Karlsruher Institut für Technologie (KIT), 2014. doi:10.5445/IR/1000087340.

[21] Vogel J, Johnson M. Natural convection during melting in vertical finned tube latent thermal energy storage systems. Appl Energy 2019;246:38–52. doi:10.1016/j.apenergy.2019.04.011.

[22] Kozak Y, Ziskind G. Novel enthalpy method for modeling of PCM melting accompanied by sinking of the solid phase. Int J Heat Mass Transf 2017;112:568–86. doi:10.1016/j.ijheatmasstransfer.2017.04.088.

[23] Bauer T. Approximate analytical solutions for the solidification of PCMs in fin geometries using effective thermophysical properties. Int J Heat Mass Transf 2011;54:4923–30. doi:10.1016/j.ijheatmasstransfer.2011.07.004.

[24] Meshgin P, Xi Y. Multi-scale composite models for the effective thermal conductivity of PCM-concrete. Constr Build Mater 2013;48:371–8. doi:10.1016/j.conbuildmat.2013.06.068.

[25] Tay NHS, Belusko M, Castell A, Cabeza LF, Bruno F. An effectiveness-NTU technique for characterising a finned tubes PCM system using a CFD model. Appl Energy 2014;131:377–85. doi:10.1016/j.apenergy.2014.06.041.

[26] Verma P, Varun, Singal SK. Review of mathematical modeling on latent heat thermal energy storage systems using phase-change material. Renew Sustain Energy Rev 2008;12:999–1031. doi:10.1016/j.rser.2006.11.002.

[27] Kuboth S, König-Haagen A, Brüggemann D. Numerical analysis of shell-and-tube type latent thermal energy storage performance with different arrangements of circular fins. Energies 2017;10. doi:10.3390/en10030274.

[28] Stückle A, Laing D, Müller-Steinhagen H. Numerical Simulation and Experimental Analysis of a Modular Storage System for Direct Steam Generation. Heat Transf Eng 2014;35:812–21. doi:10.1080/01457632.2013.828556.

[29] The Dow Chemical Company. Syltherm 800 technical data sheet 2001. www.dow.com.

[30] Wagner W, Cooper JR, Dittmann A, Kijima J, Kretzschmar H-J, Kruse A, Mareš R, Oguchi K, Sato H, et al. The IAPWS Industrial Formulation 1997 for the Thermodynamic Properties of Water and Steam. J Eng Gas Turbines Power 2000;122:150–84. doi:10.1115/1.483186.

[31] Wagner H-J, Kretzschmar W. IAPWS Industrial Formulation 1997 for the Thermodynamic Properties of Water and Steam. In: International Steam Tables. Springer Berlin Heidelberg; 2008. doi:10.1007/978-3-540-74234-0_3.

[32] Woldesemayat MA., Ghajar AJ. Comparison of void fraction correlations for different flow patterns in horizontal and upward inclined pipes. Int J Multiph Flow 2007;33:347–70. doi:10.1016/j.ijmultiphaseflow.2006.09.004.

[33] Xu Y, Fang X, Su X, Zhou Z, Chen W. Evaluation of frictional pressure drop correlations for two-phase flow in pipes. Nucl Eng Des 2012;253:86–97. doi:10.1016/j.nucengdes.2012.08.007.

[34] Friedel L. Improved friction pressure drop correlations for horizontal and vertical two-phase pipe flow. European two-phase flow group meeting, Ispra 1979;18:485–91.

[35] Müller-Steinhagen H, Heck K. A simple friction pressure drop correlation for two-phase flow in pipes. Chem Eng Process Process Intensif 1986;20:297–308. doi:10.1016/0255-2701(86)80008-3.

[36] Winterton RHS. Where did the Dittus and Boelter equation come from? Int J Heat Mass Transf 1998;41:809–10. doi:https://doi.org/10.1016/S0017-9310(97)00177-4.

[37] Hänninen M, Ylijoki J. The constitutive equations of the APROS six-equation model. Manual of APROS Version 5.09; 2007.

[38] Chen SL, Gerner FM, Tien CL. General Film Condensation Correlations. Exp Heat Transf 1987;1:93–107. doi:10.1080/08916158708946334.

[39] Groeneveld DC, Shan JQ, Vasić AZ, Leung LKH, Durmayaz A, Yang J, Cheng SC, Tanase A. The 2006 CHF look-up table. Nucl Eng Des 2007;237:1909–22. doi:10.1016/j.nucengdes.2007.02.014.

[40] Bauer T, Laing D, Tamme R. Characterization of sodium nitrate as phase change material. Int J Thermophys 2012;33:91–104. doi:10.1007/s10765-011-1113-9.

[41] Voller V, Prakash C. A fixed grid numerical modelling methodology for convection-diffusion mushy region phase-change problems. Int J Heat Mass Transf 1987;30:1709–19. doi:10.1016/0017-9310(87)90317-6.

[42] Brent AD, Voller VR, Reid KJ. Enthalpy-Porosity Technique for Modeling Convection-Diffusion Phase Change: Application to the Melting of a Pure Metal. Numer Heat Transf 1988;13:297–318. doi:10.1080/10407788808913615.

[43] Voller VR, Swaminathan CR. General Source-Based Method for Solidification Phase Change. Numer Heat Transf Part B 1991;19:175–89. doi:10.1080/10407799108944962.

[44] ANSYS Inc. ANSYS 15 Fluent User's Guide 2015.

[45] Versteeg HK, Malalasekera W. An introduction to computational fluid dynamics: The Finite Volume Method. 2nd ed. 2007.

[46] Patankar S. NUMERICAL HEAT TRANSFER AND FLUID FLOW. Hemisphere Publishing; 1980.

[47] APROS - Process Simulation Software. VTT Technical Research Centre of Finland Ltd. 2014. www.apros.fi.